Design of A Variable-Stiffness Ankle-Foot Orthosis Emulator

A THESIS

SUBMITTED TO THE FACULTY OF

THE UNIVERSITY OF MINNESOTA

BY

RACHEL ANDERSON

IN PARTIAL FULFILLMENT OF THE
REQUIREMENTS

FOR THE DEGREE OF

MASTER OF MECHANICAL ENGINEERING

ADVISOR: WILLIAM DURFEE

AUGUST 2020

Abstract

Ankle-foot orthoses (AFOs) are passive devices used to improve gait in children with cerebral palsy. They are characterized by a torsional stiffness and ankle neutral angle. For this project, a lightweight ankle exoskeleton was designed to emulate the spring-like behavior of a traditional AFO for a wide range in torsional stiffnesses and neutral angles. This was achieved by utilizing the principles of a cantilever beam to generate a desired stiffness profile and lightweight hydraulics to transmit forces from a power source worn at the waist to the device at the ankle. The proposed device was evaluated using FEA and CAD modeling and met most design requirements. The next stage of design evaluation will involve a physical prototype before the final product is implemented in a clinical trial at Gillette Children's Specialty Healthcare.

Contents

List of Figures v

List of Tables vii

1 Introduction 1

1.1 Background and Motivation 1

1.2 Review of AFOs 2

1.2.1 Passive AFOs 2

1.2.2 Active AFOs 5

1.3 Project Objective 7

2 AFO Emulator Design 8

2.1 Design Requirements 8

2.2 Design Overview 9

2.3 Cantilever Beam Approach 12

2.3.1 Beam Theory 12

2.3.2 Concept Defined 13

2.3.3 Methods Derived 16

2.3.4 Design Optimized 20

2.3.5 Concept Validation 22

2.4 Transmission Design 23

2.4.1 Cylinder Design 24

2.4.2 Hydraulic System Approaches 25

2.4.3 System Specifications 27

2.4.4 Component Selection 30

2.5 Ankle Exoskeleton Design 30

2.5.1 Limb Mount 31
2.5.2 Beam 31
2.5.3 Beam Mount & Foot Plate 32
2.6 Total Device Stiffness 35
3 Methods for Design Evaluation 36
3.1 Weight Evaluation 36
3.2 Stiffness Evaluation 37
4 Results 37
4.1 Beam Mount Stress Analysis 37
4.2 Weight Assessment 37
4.3 Stiffness Assessment 39
4.3.1 Beam Verification 39
4.3.2 Total Device Stiffness 41
4.4 AFO Performance Comparison 43
5 Discussion 44
5.1 Design Requirements 44
5.2 Design Limitations 45
5.3 Alternative Directions 46
5.4 Future Work 46
References 46
Appendices 52
Appendix A: Proof of Concept 52
Appendix B: Optimization Results 54
Appendix C: Bill of Materials 55
Appendix D: Part Specifications 56

Miniature Pump 56
Solenoid On-off Valves 57
Miniature Linear Rails 58
Appendix E: Seal Design 59

List of Figures

Figure 1: Drawing demonstrating the principle of stiffness (K) and neutral angle (θ). 1
Figure 2: Posterior leaf spring (left), solid (middle), and hinged (right) AFOs [21]. 3
Figure 3: Frequency of AFO neutral angles and stiffnesses prescribed at GCSH [19]. 4
Figure 4: Measured peak deflections and torques of AFOs at GCSH. 4
Figure 5: Schematic of the VSO developed by the Neurobionics Lab. 5
Figure 6: The Caplex ESO-001 by Humotech [36]. 6
Figure 7: The Hydraulic-Powered AFO designed in the Human/Machine Design Lab. 6
Figure 8: BRUCE data for the PHAFO and the AFO [19]. 7
Figure 9: Autotuner concept art. 8
Figure 10: Overview of Autotuner system 9
Figure 11: Isometric (top) and top (bottom) views of the Autotuner ankle assembly. 10
Figure 12: Line drawing of the Autotuner with callouts described in Table 2 11
Figure 13: Rendering of the final beam design with variable cross-section. 12
Figure 14: Example of a cantilever beam deflected under load f. 12
Figure 15: Concept art of cantilever approach to a variable stiffness AFO 14
Figure 16: Stage definition for varying the loading on a cantilever beam 14
Figure 17: Definitions for beam cross-section dimensions 18
Figure 18: Bounds imposed on the solution plotted in the $lmin - lmax$ space. 21
Figure 19: Solution space with solution selected for this project. 22
Figure 20: Length v. stiffness curves for beams with constant and variable profiles. 23
Figure 21: Transmission concepts considered for this project. 23
Figure 22: Rendered hydraulic cylinder for transmission 24
Figure 23: Hydraulic cylinder design and working principle. 24
Figure 24: Component callout for custom hydraulic cylinder. 25
Figure 25: Hydraulic schematic for reversible pump circuit. 26
Figure 26: Hydraulic schematic for irreversible pump circuit. 27
Figure 27: Description of hydraulic sub-circuit pressures. 28
Figure 28: Peak pressures in cylinders of varying bore diameter. 29
Figure 29: Concept art of exoskeleton with component callouts. 30

Figure 30: Side (right) and top (left) views of the beam. 31
Figure 31: Model of the foot plate. 32
Figure 32: Base solid of beam mount used for topology optimization. 33
Figure 33: Lever simplification used to solve for forces in beam mount. 33
Figure 34: Topology optimization results and resulting model of beam mount. 34
Figure 35: Spring simplification of compressed fluid in hydraulic cylinder. 36
Figure 37: Mass breakdown of the Autotuner exoskeleton. 38
Figure 38: Comparison of Autotuner mass with AFOs prescribed at GCSH. 39
Figure 40: ANSYS deflection results plotted against analytical solutions. 40
Figure 41: Stiffness v. beam length for analytical solution and ANSYS data. 41
Figure 42: Difference between beam stiffness and total device stiffness for varying r. 42
Figure 43: Analytical and total device stiffness curves in the PF and DF directions. 42
Figure 44: ANSYS results from cyclic loading on beam. 43
Figure 45: Low-fidelity prototype of the Autotuner. 52
Figure 46: Stiffness data results from proof-of-concept testing. 53
Figure 47: Thickness profile calculated using the beam optimization. 54
Figure 48: Stiffness v. beam length relationship for the optimized I-beam. 54
Figure 49: Radial clearance guidelines for varying fluid pressures. 59
Figure 50: Definition of radial clearance in this sealing application. 59

List of Tables

Table 1: Design requirements for the Autotuner. 9
Table 2: Description of callouts from Figure 12. 11
Table 3: Nomenclature used in derivations. 15
Table 4: Assumptions made in derivations. 15
Table 5: Constraints imposed on the stage and beam design optimization. 21
Table 6: Stage and beam properties determined using optimization. 22
Table 7: Combinations of hydraulic approaches to consider. 25
Table 8: Values used in pressure analysis. 28
Table 9: Results of pressure analysis. 28
Table 10: Required pressure and flow specifications for pump and valves. 29
Table 11: Pump and valves selected for hydraulic circuit. 30
Table 12: Stiffness values tested in ANSYS beam assessment. 39
Table 13: Design requirement verification. 45

1 Introduction

1.1 Background and Motivation

Cerebral palsy (CP) is a group of neurological disorders characterized by stiff muscles, lack of muscle coordination, heightened reflexes, weakness, and abnormal gait; consequently, a person's ability to maintain proper posture and balance is impacted [1], [2]. In the U.S., CP is present in 3.3 out of 1000 births and 4 out of 1000 worldwide, making it the most prevalent motor disability in childhood and the leading cause of severe physical disability [1]–[4]. A sample of children with CP eight years of age showed that 58% could walk independently, 11% needed to use an assistive device, and 31% had limited mobility [3].

The most common device used by nearly 50% of children with CP is an ankle-foot orthosis (AFO) [5], [6]. An AFO's purpose is to enhance gait by improving ankle-foot functional synergies [5]. AFOs have been shown to improve gait in children overall [5], [7]–[9]; however, specific results of AFO efficacy vary [10]–[12]. An AFO is characterized by its stiffness, shape, and neutral angle, and the assignment of these characteristics is termed "tuning" (Figure 1). Evidence suggests that proper tuning of an AFO can improve the overall effectiveness of the device and mitigate adverse outcomes [13]–[15]. Both simulation studies [16] and clinical practice [17], [18] support the notion that AFO tuning is necessary, demonstrating specifically that stiffness and neutral angle are important factors contributing to AFO efficacy to improve gait.

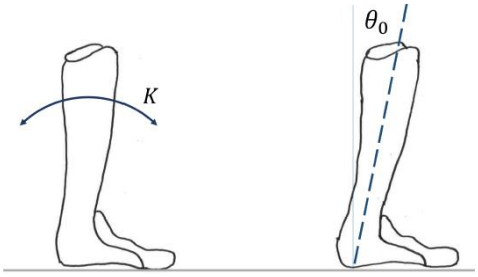

Figure 1: Drawing demonstrating the principle of stiffness (K) and neutral angle (θ).

Gillette Children's Specialty Healthcare (GCSH) is a leading provider of AFOs: of 4,000 lower-limb orthotic devices prescribed by GCSH in 2019, 2,000 were AFOs [19]. As experts in the field, researchers at GCSH are aware of the many challenges and limitations associated with AFOs. A study by Ries found that only 37% of prescriptions maximize the benefits of an AFO, while 28% of prescriptions impacted the child's outcome negatively [20]. Imperfect device tuning can lead to muscle atrophy and wear noncompliance, increasing the likelihood of adverse effects [12], [21]. Methods used to prescribe AFOs are largely based on practitioner skill, and prescription quality can depend on access to a motion capture system [21]; consequently, prescription outcomes vary widely among healthcare providers and the process is not standardized [22]. Even though AFO tuning has been proven to significantly impact gait outcomes in children with CP, the prescription process lacks the structure required to assign a definitive stiffness value to a device. A study conducted by Kane demonstrated that AFO prescriptions are largely determined by clinician and parental opinion, expertise, and preferences, and financial influences, rather than a child's individual factors [23]. The prescription process is both costly and time consuming for families, as growing children often require a new AFO every 12 - 18 months [21]. Furthermore, improper design of an AFO can lead to higher lifetime healthcare costs for individuals with CP as a direct result of increased corrective prescriptions and surgeries and indirectly from reduced mobility over the patient's lifetime. It is therefore imperative that an efficient and standardized method be developed to pinpoint the optimal AFO stiffness and neutral angle requirements for a child to achieve the best possible outcome. The device described in this report is intended to fill this need.

1.2 Review of AFOs

1.2.1 Passive AFOs

AFOs are constructed in a variety of ways, each targeting certain gait issues such as excessive ankle plantar-flexion, knee buckling and hyperextension, short stride length, and slow speed. Common examples of AFOs include posterior leaf spring (PLS), one-piece solid AFO (SAFO), and two-piece hinged AFOs (HAFO) (Figure 2). Commonly

prescribed at GCSH is the SAFO, which is used to control and correct knee hyperextension as well as other gait challenges common to CP [21].

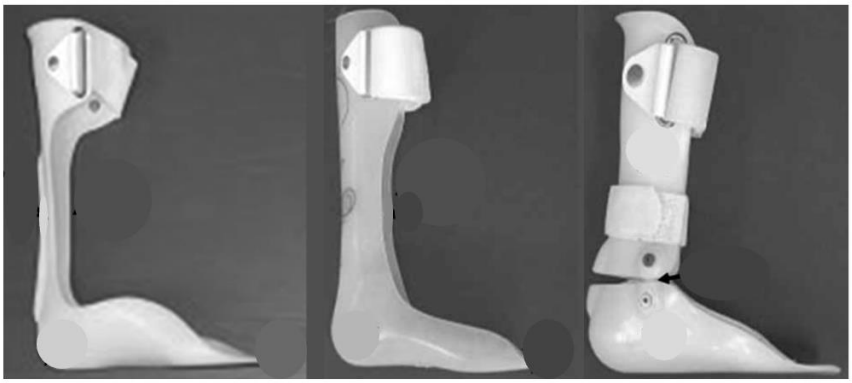

Figure 2: Posterior leaf spring (left), solid (middle), and hinged (right) AFOs [21].

AFOs are typically constructed from polypropylene, low-density polyethylene (LDPE), high-density polyethylene (HDPE) or a combination to achieve the desired strength, stiffness, and shape [15], [21]. The stiffness of an SAFO or PLS is lessened by removing material at the ankle joint. In contrast, hinged AFOs are adjusted by tightening a torsional spring. The neutral angle of an SAFO or PLS is set when the orthotist takes a cast of the patient's limb. Because of this, the precision of the AFO manufacturing process is highly dependent on the orthotist's level of expertise [23]. Advanced techniques in manufacturing are currently being developed to generate AFOs with precise stiffness and neutral angle properties [24], [25]; selective laser sintering has shown promising results but remains experimental at this time [26].

There exists a number of methods to quantify the stiffness of an AFO [27]. A Bi-articular Reciprocating Universal Compliance Estimator (BRUCE) is commonly used to obtain values for AFO stiffness, maximum torque, and range-of-motion [28]. GCSH regularly uses BRUCE in conjunction with a GAIT motion capture system to obtain estimates for AFO stiffness and neutral angle. GCSH evaluated 183 SAFOs worn by people of the average age 11.8 ± 4.5 years (5th - 95th percentile range of [6.6, 17.7]) and found that the stiffness of an AFO ranges from 0.1 to 16.1 Nm/deg (5th - 95th percentile range of [0.2, 7.4]) with an average stiffness of 1.7 Nm/deg. The average neutral angle prescribed at

GCSH was 5.1 ± 4.9 deg of dorsiflexion in the range of 6.5 deg of plantarflexion to 20.7 deg of dorsiflexion (Figure 3) [19].

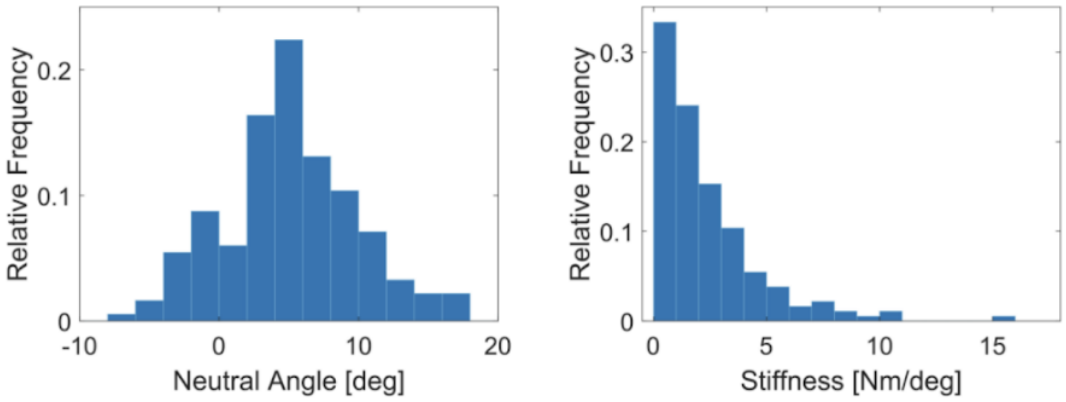

Figure 3: Frequency of AFO neutral angles and stiffnesses prescribed at GCSH [19].

Additionally, the maximum torque generated over the gait cycle by each AFO was measured. It was concluded that in order to emulate 95% of the AFOs at GCSH, an AFO emulator must be able to generate between 66 Nm of plantarflexion torque and 21 Nm of dorsiflexion torque (Figure 4).

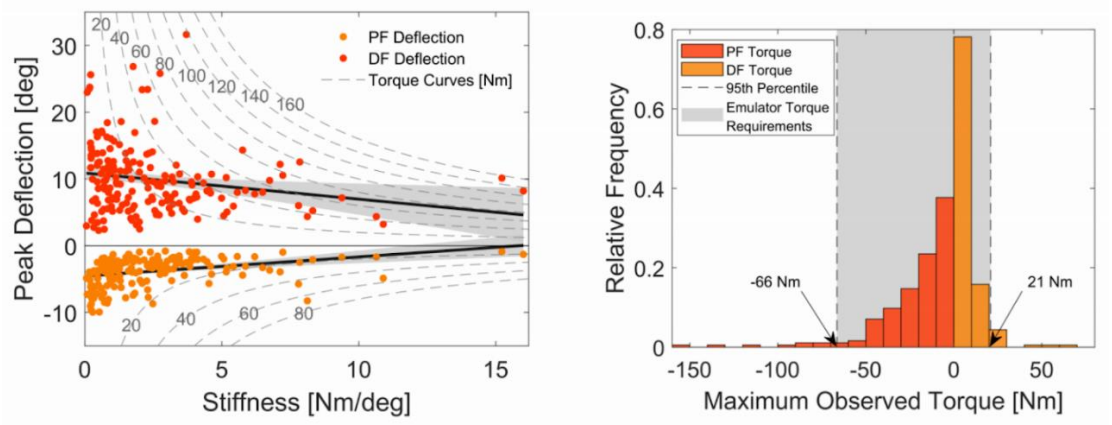

Figure 4: Measured peak deflections and torques of AFOs at GCSH.

Typical AFO weight and height measurements were collected from a separate sample of 32 patients at GCSH ranging from 7 to 17 years of age. AFO types measured included SAFO, HAFO, and PLS. The average mass of the AFOs in this set was 237 +/- 48 g (with

range [150, 400]), and the average height of the AFOs was 31 +/- 3 cm (with range [26, 41]).

1.2.2 Active AFOs

Many powered devices have been developed to correct gait abnormalities in adult patients [29], [30]. Actuated AFOs (AAFOs) are designed to modulate the joint impedance over the walking cycle to best meet the needs of the patient [31]–[34]. Recently, the Neurobionics Lab at the University of Michigan is developing a Variable Stiffness Orthosis (VSO) intended for adult daily wear that uses a cam-based transmission to adjust the loading on a leaf-spring mounted at the posterior ankle (Figure 5) [35]. This device is noted for its specific aim at emulating the functional behavior of plastic AFOs.

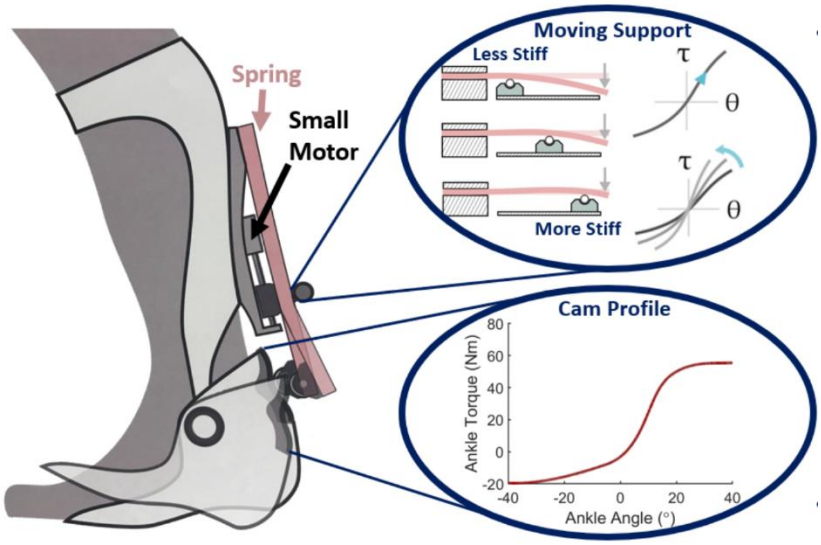

Figure 5: Schematic of the Variable Stiffness Orthosis developed by the Neurobionics Lab [35].

The Caplex ESO-001 by Humotech is a tethered, variable compliance, ankle exoskeleton intended to aid the AFO prescription process (Figure 6). The device is capable of generating 180 Nm of plantarflexion torque and 1.5 Nm of dorsiflexion torque, and the portion at the ankle weighs approximately 1.4 Kg with a shoe [36]. While useful for evaluating the impact of stiffness on gait, this device is heavier than a passive AFO and would need to be modified to meet the DF torque requirements at GCSH.

Figure 6: The Caplex ESO-001 by Humotech [36].

The Pediatric Hydraulic-Powered AFO (PHAFO) was developed in the Human/Machine Design Lab for a prior study with GCSH (Figure 7). The device uses hydraulic-actuated pulleys at the ankle in feedback with force and angle sensors to modulate the stiffness of the joint. The PHAFO is also able to alter the neutral angle of the ankle about a fixed pin joint. Due to the hydraulic requirements for the system, the device is tethered to a mobile hydraulic power unit and weight at the ankle is 1.4 Kg with a shoe.

Figure 7: The Hydraulic-Powered AFO designed in the Human/Machine Design Lab.

The stiffness of the PHAFO was evaluated using BRUCE and directly compared to an AFO. While the PHAFO was able to exhibit a similar torque-angle profile as the traditional AFO, the device demonstrated a more linear behavior and larger hysteresis than the plastic AFO (Figure 8). This may be attributed to the sensor-based nature of the PHAFO and the fixed axis of ankle rotation set by the pin joint.

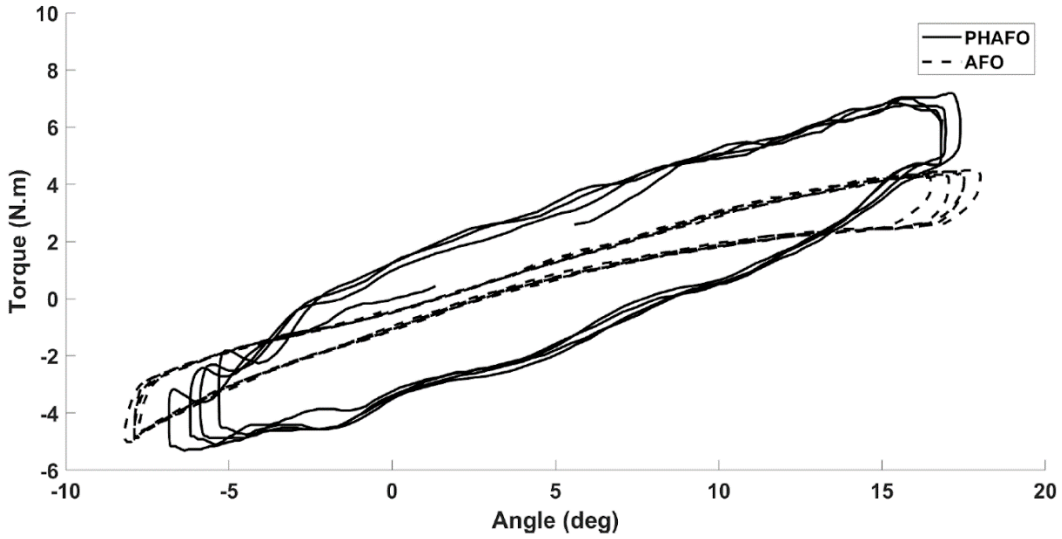

Figure 8: BRUCE data for the PHAFO and the AFO [19].

Like the PHAFO, the VSO designed at the University of Michigan and Humotech's ESO-001 set the joint movement about a fixed pin joint. This creates slightly different functional behavior than the rolling joint of a SAFO and should be considered when designing an AFO emulator. Currently, an untethered, pediatric, lightweight device that mimics the rolling-joint behavior of an SAFO with variable compliance and neutral angle has not been developed.

1.3 Project Objective

To improve the AFO prescription process, a portable, lightweight AFO emulator will be developed (Figure 9). The long-term objective of the project is to integrate machine learning with the exoskeleton device to actively tune the stiffness and neutral angle such that the optimal prescription is achieved prior to manufacturing a plastic AFO. The

objective of this project was to design a method for controlling the stiffness and neutral position of the ankle in such a way that the device is more lightweight than the PHAFO, has a power source worn at the hip, and demonstrates similar functional torque-angle behavior to a plastic AFO.

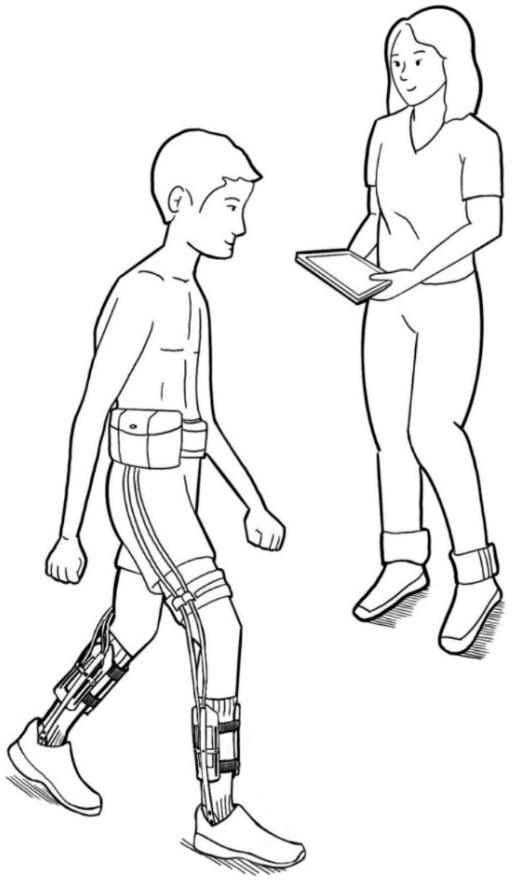

Figure 9: Autotuner concept art.

2 AFO Emulator Design

2.1 Design Requirements

The AFO emulator, called the ‘Autotuner’, must meet four design criteria derived from the data on AFO prescriptions presented earlier in this report. To achieve the objective of this project, the exoskeleton of the device must be significantly lighter than prior technology to better match the weight of a traditional AFO. The device must also be untethered and must

be able to be worn and carried by children of the typical age range at GCSH. Functionally, the device must be able to emulate a wide range of AFO stiffnesses and neutral angles while mimicking the rolling-joint behavior of an SAFO. The design requirements to be followed are provided in Table 1.

Table 1: Design requirements for the Autotuner.

Requirement	Description	Value
Stiffness Range	Must generate stiffnesses prescribed at GCSH	1 Nm/deg to 10 Nm/deg
Neutral Angle Range	Must generate neutral angles prescribed at GCSH	5 deg plantarflexion to 15 deg dorsiflexion or a 20 deg range
Weight at Ankle	Must be close in weight to plastic AFOs	AFO mass: 237 g
Patient Sizes	Must fit children	AFO height: 31 cm

2.2 Design Overview

The Autotuner has four functional groups: the ankle exoskeleton, the transmission, the power supply, and the controller (Figure 10). This project focused on the design of the exoskeleton and transmission. A render of the ankle assembly is shown in Figure 11 and described in Figure 12 and Table 2.

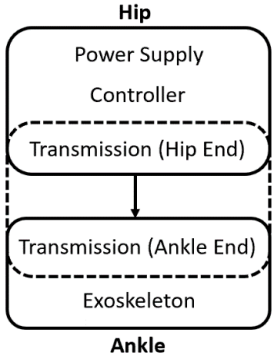

Figure 10: Overview of Autotuner system.

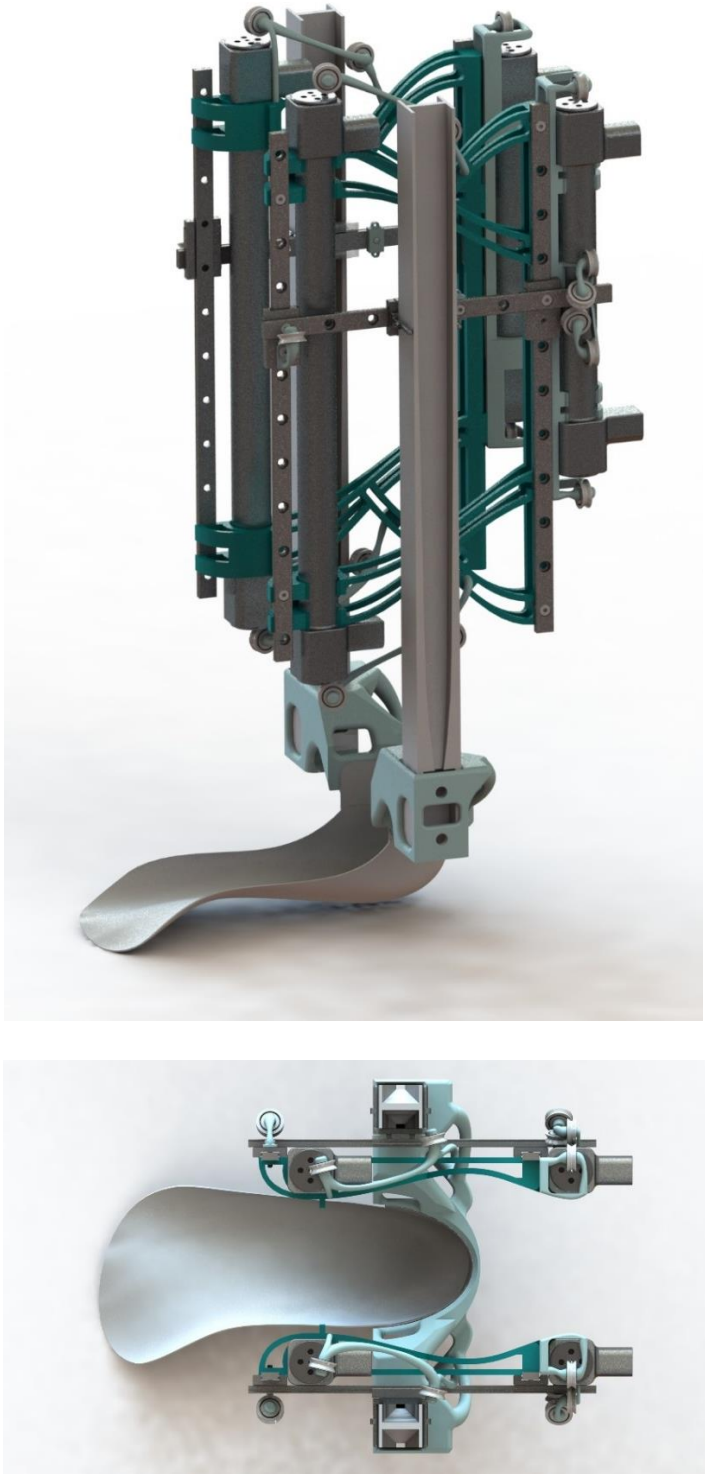

Figure 11: Isometric (top) and top (bottom) views of the Autotuner ankle assembly.

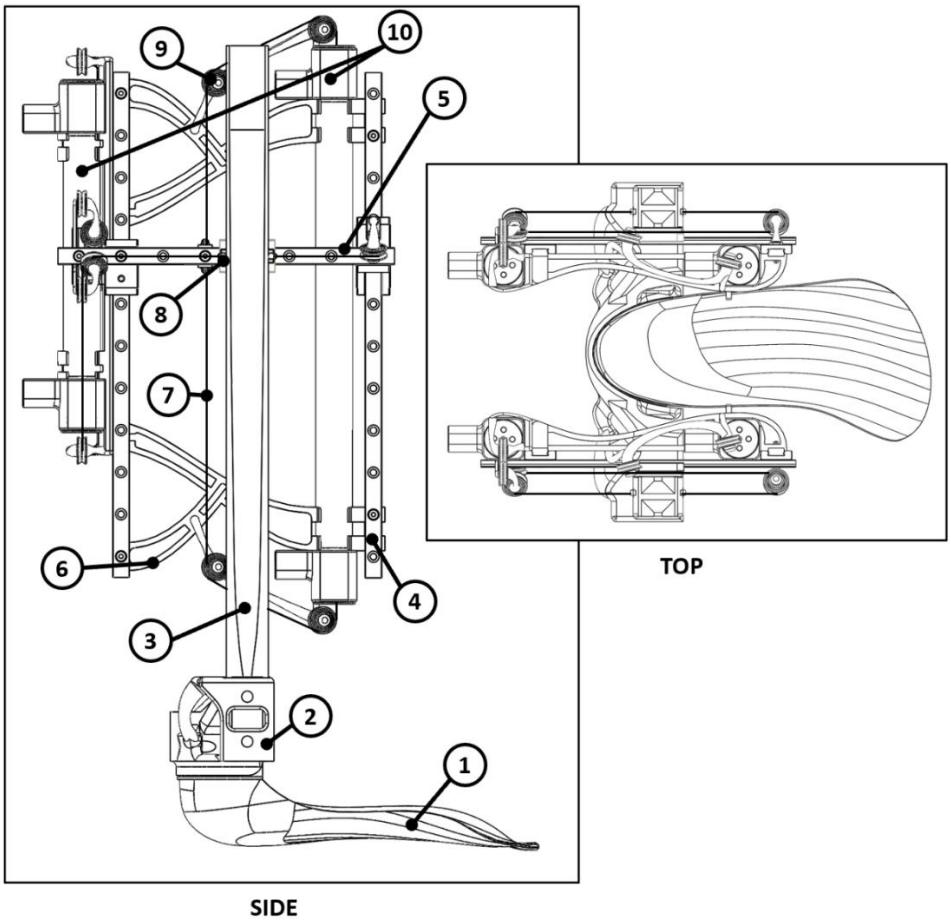

Figure 12: Line drawing of the Autotuner with callouts described in Table 2 .

Table 2: Description of callouts from Figure 12.

#	Name	Description
1	Foot Plate	Mimics the foot portion of an AFO – can be made in many sizes
2	Beam Mount	Fixes the end of the beam to the foot plate
3	Beam	Mimics the compliance of an AFO
4	Vertical Slide Rail	Moves the loading position on the beam to adjust the device stiffness
5	Horizontal Slide Rail	Moves the loading position on the beam to adjust the neutral angle
6	Limb Mount	Holds the stage components to the ankle
7	Cable	Transfers piston motion to move the load point on the stage
8	Load Point	Applies a load to the beam
9	Pulley	Directs cable motion on stage
10	Hydraulic Cylinders	Transmit fluid motion at the hip to motion at the stage

2.3 Cantilever Beam Approach

Two cantilever beams mounted medially and laterally to the foot of the device create variable ankle compliance that can be dynamically tuned to optimize the wearer's gait. This is achieved by adjusting the position of the loading on the beam relative to its fixed end. The cross-section of the beam varies along its length to maximize the achievable stiffness range over a desired beam length (Figure 13). The theory behind this method is described in the following sections.

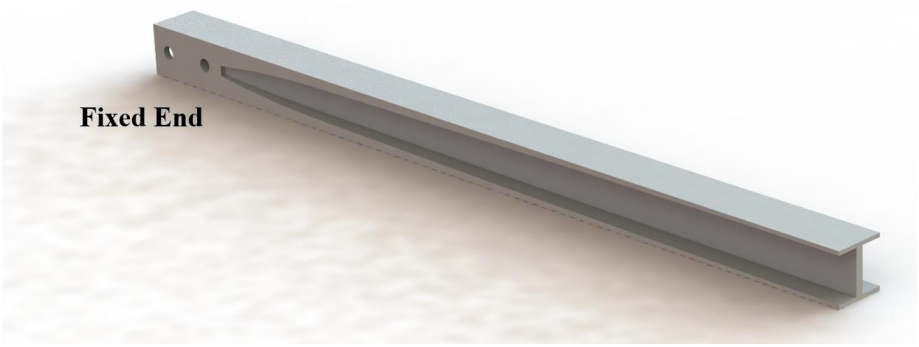

Figure 13: Rendering of the final beam design with variable cross-section.

2.3.1 Beam Theory

A cantilever is a beam that has a fixed end and a free end. Castigliano's second theorem states that the displacement along a beam in the direction of load f is equal to the derivative of the strain energy of the beam with respect to the load f as long as the structure is linearly elastic (1) [37]. For a cantilever beam with a point load f at position l along the beam, Castigliano's second theorem can be used to relate the deflection at position l, δ, to the moment on the beam, the material of the beam, and the shape of the beam (Figure 14).

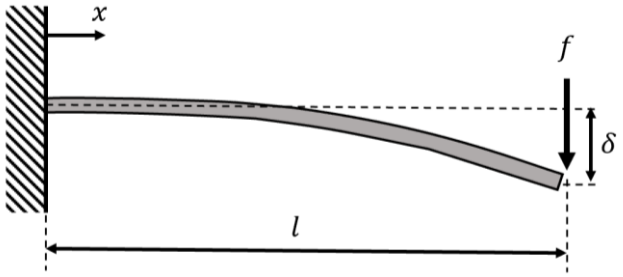

Figure 14: Example of a cantilever beam deflected under load f.

$$\delta = \int_0^l \frac{f(l-x)^2}{EI(x)}\,dx \tag{1}$$

This equation can be applied to a cantilever beam of length l with constant cross section and end load f, resulting in the standard expression for end deflection of a cantilever under fixed end loads (2).

$$\delta = \frac{fl^3}{3EI} \tag{2}$$

The beam stiffness (force over deflection) is proportional to the flexural rigidity of the beam (EI) and inversely proportional to the cube of the length of the beam. A shorter beam will be much stiffer than a longer beam (3).

$$K_{beam} = \frac{f}{\delta} = \frac{3EI}{l^3} \tag{3}$$

2.3.2 Concept Defined

The cantilever beam can be applied to the basic principle of an AFO, where the fixed point of the beam is located at the foot and a load is applied by the ankle. In a traditional AFO, the stiffness of the joint is set by changing the amount of material present, or in other words, changing the moment of inertia of the 'beam'. This concept can be expanded to a variable compliance model where the stiffness of the beam is instead controlled by the position of the loading on the beam relative to the fixed end. Using this approach, the rolling-joint behavior and passivity of a traditional AFO are achieved and the damping properties of typical AFO materials are conserved.

A design where two cantilever beams are fixed to the medial and lateral sides of a foot and loaded at a point fixed to the ankle was chosen as the basis for this device (Figure 15). In this model, the total force of the ankle on the orthosis, F_{ankle}, is equal to the sum of the loading on each beam, f, and the required force to deflect the device increases as f moves closer to the fixed end. From this, a model for the torsional stiffness of the exoskeleton as a function of the "effective beam length" was derived.

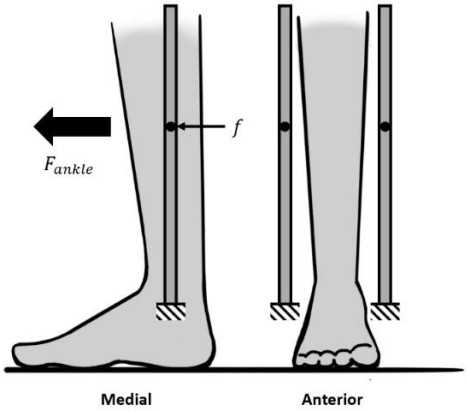

Figure 15: Concept art of cantilever approach to a variable stiffness AFO.

To fully define the system, the exoskeleton is approached as a single-beam system and divided into three functional groups: the fixed support (which is rigidly attached to the wearer's foot), the beam, and the stage (which is rigidly attached to the wearer's lower leg). The stage is connected to the beam by a movable 'load point' and is used to change the position of the loading on the beam relative to the fixed support (Figure 16).

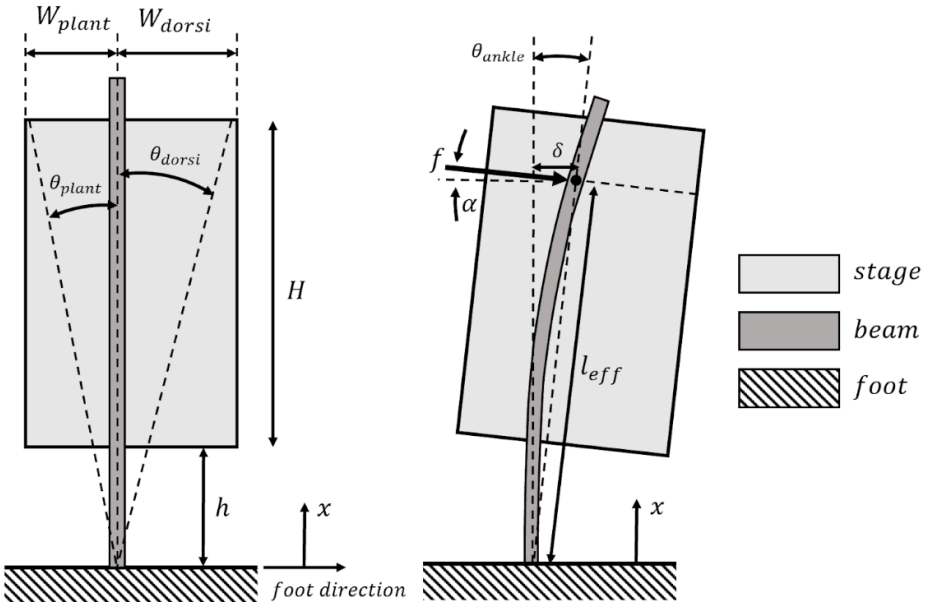

Figure 16: Stage definition for varying the loading on a cantilever beam.

By coupling the beam with the lower leg in this way, it is possible to achieve a range of both joint stiffnesses and neutral angle positions. Because the stage is rigidly mounted to

the limb, motion of the load point perpendicular to the beam changes the relative angle between the stage centerline and the ground normal, thereby changing the neutral angle of the joint. A mockup was developed as proof of concept and results are detailed in Appendix A. The beam and stage properties listed in Table 1 must be selected to meet the stiffness and angle requirements defined for the device within the dimensions of a child's lower leg. Assumptions are provided in

Table 4.

Table 3: Nomenclature used in derivations.

Symbol	Description	Units
K_{max}, K_{min}	Maximum/Minimum Device Stiffness	Nm/deg
K_{ankle}	Ankle/Device Stiffness	Nm/deg
$\theta_{dorsi}, \theta_{plant}$	Maximum Neutral Angle (Dorsiflexed/Plantarflexed)	deg
T_{ankle}, F_{ankle}	Torque and associated force output from ankle	Nm, N
θ_{ankle}	Angle of ankle	deg
α	Angle between force on beam and horizontal	deg
x	Distance Along Beam from Fixed Point	m
E	Young's Modulus	GPa
$I(x)$	Moment of Inertia	m^4
l_{max}	Maximum Length (associated with minimum stiffness)	m
l_{min}	Minimum Length (associated with maximum stiffness)	m
l_{eff}	Effective Length of Beam	m
f	Force Applied to Beam	N
H	Stage Height	m
h	Distance of Stage from Fixed Point	m
W_{dorsi}, W_{plant}	Width of Stage in Dorsiflexed /Plantarflexed Direction	m
W	Width of Stage	m

Table 4: Assumptions made in derivations.

1	θ_{ankle} is small
2	α is approximately zero
3	Beam is slender

2.3.3 Methods Derived

It is known that the torque required at the ankle is the total force applied to the device by the ankle, F_{ankle}, multiplied by the moment arm, which by (Figure 16) is defined as the effective beam length. The ankle force is divided between the medial and lateral beams, so (4) is derived.

$$T_{ankle} = 2fl_{eff} \tag{4}$$

From assumption 1 in

Table 4, the angle of the ankle can be related to the beam deflection by (5). The ankle stiffness is the torque output of the ankle over the ankle angle, giving (6).

$$\theta_{ankle} \approx \frac{\delta}{l_{eff}} \tag{5}$$

$$K_{ankle} = \frac{T_{ankle}}{\theta_{ankle}} = \frac{2fl_{eff}^2}{\delta} \tag{6}$$

By Castigliano's Theorem, the beam deflection at the load point can be written as a function of the effective length of the beam, resulting in a relationship between the stiffness of the beam and the effective length (7). A relationship between the desired length-stiffness profile of the beam and the beam's moment of inertia was also derived. For a beam with an unchanging cross section, the stiffness of the exoskeleton as a function of the position of the load point relative to the fixed end can be written simply (8). To meet the requirements defined for this project, it was necessary to explore the capabilities of a beam with a varying moment of inertia. A novel method was developed to find the variable moment of inertia required for an optimal stiffness profile.

$$K_{ankle} = 2l_{eff}^2 \left\{ \int_0^{l_{eff}} \frac{\left(l_{eff} - x\right)^2}{EI(x)} dx \right\}^{-1} \tag{7}$$

$$K_{ankle} = \frac{6EI}{l_{eff}} \tag{8}$$

The moment of inertia is determined by the cross-section shape and dimensions at any point along the beam. It may be described generally by a polynomial function in terms of the position along the beam relative to the fixed beam base, x, where I_0 is the moment of inertia at the base (9). Constraints are imposed on this relationship to ensure that a manufacturable beam is derived. Using this definition for the moment of inertia, the stiffness of the ankle can be rewritten solely as a function of the effective beam length (10), resulting in the driving equation for the design optimization.

$$I(x) = I_0(ax + 1)^b \tag{9}$$

$$\forall\{\, a \in \mathbb{R} \mid a < 0 \,\}$$

$$K_{ankle} = 2l_{eff}^2 \left\{ \int_0^{l_{eff}} \frac{\left(l_{eff} - x\right)^2}{EI_0(ax + 1)^b} dx \right\}^{-1} \tag{10}$$

To reduce the set of possible solutions, the cross-sectional shape of the beam must be chosen. After considering typical beam shapes, rectangle and I-beam shapes were selected for their flat edges and ease of manufacture (Figure 17). The constant w and variable t were assigned to each shape such that univariate solutions could be easily derived. An additional variable r was assigned as a free choice that could be used to tune the shape of the beam.

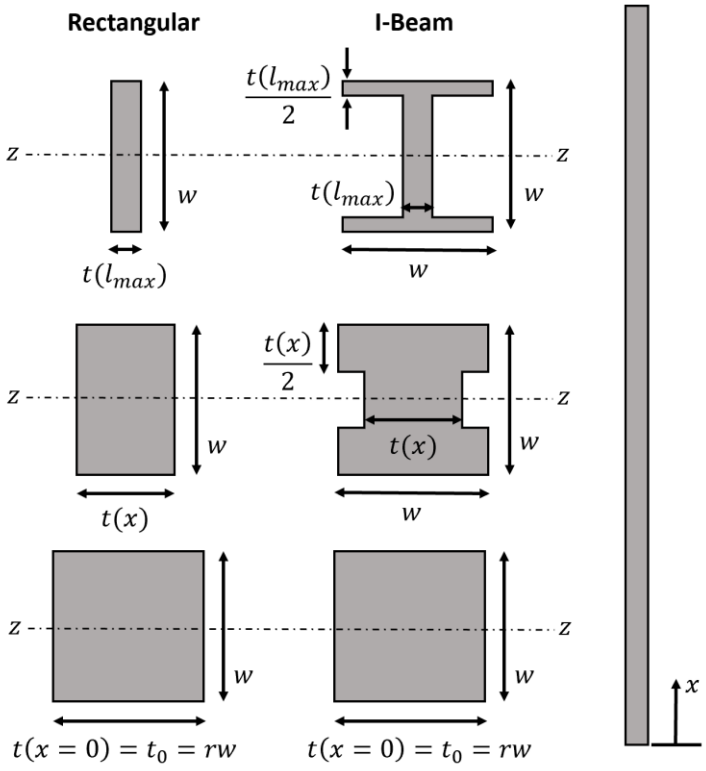

Figure 17: Definitions for beam cross-section dimensions and how they vary along the beam length.

The rectangular cross section may be used to demonstrate the beam design process. The moment of inertia for the rectangular beam about the $z-z$ axis is provided in (11). Combining (11) with (9), the expression for $t(x)$ is derived (12).

$$I_R = \frac{tw^3}{12} \tag{11}$$

$$t(x)|_R = \frac{12I_0}{w^3}(ax+1)^b \tag{12}$$

Similarly, the varying I-beam dimension may be derived. The moment of inertia for the I-beam about the $z-z$ axis is provided in (13). As this expression is fourth order with respect to t, the four possible solutions must be examined. The roots of this polynomial are provided in (14).

$$I_I = \frac{t}{12}(-t^3 + 4t^2w - 6tw^2 + 4w^3) \tag{13}$$

$$t = \left\{w \pm (w^4 - 12I_I)^{\frac{1}{4}}\right\}, \left\{w \pm \left(-(w^4 - 12I_I)^{\frac{1}{2}}\right)^{\frac{1}{2}}\right\} \tag{14}$$

Because the second set of solutions are always imaginary, they can be ignored. By the constraint that $t \leq w$ the only solution to consider is defined by (15).

$$t(x)|_I = w - \left(w^4 - 12(I_0(ax+1)^b)\right)^{\frac{1}{4}} \tag{15}$$

Here, the initial moment of inertia I_0 is driven by the initial thickness t_0, which is defined as a ratio r of the beam width w. By defining w and t in this way, the number of variables needed to solve is reduced; correspondingly, the initial moment of inertia I_0 is easily derived for both cases (16, 17).

$$I_{0,R} = \frac{rw^4}{12} \tag{16}$$

$$I_{0,I} = \frac{rw^4}{12}(-r^3 + 4r^2 - 6r + 4) \tag{17}$$

It can be proven that the I-beam will result in a more efficient solution than the rectangular beam by calculating the shape factor. The shape factor of the cross section is provided in (18) and represents the ratio of the stiffness of any shaped beam to that of a solid circular cross section [38]. Here, A is the area of the cross section, and I is the moment of inertia.

$$SF = \frac{4\pi I}{A^2} \tag{18}$$

For an I-beam and a rectangular beam with the same area and dimension w, the ratio between the shape factors can be derived (19). Because $A \leq w^2$, it can be proven by the relationship in (20) that the shape factor for the I-beam is always greater than or equal to that of the rectangle cross-section, no matter how t varies in each. This proves that the I-beam will always achieve the same stiffness as a given rectangular beam using less material.

$$\frac{SF_I}{SF_R} = \frac{2w^2 - A}{w^2} = 2 - \frac{A}{w^2} \tag{19}$$

$$1 \leq \frac{SF_I}{SF_R} \leq 2 \tag{20}$$

2.3.4 Design Optimized

An optimization was constructed to ultimately find the I-beam parameters that could produce the desired range in stiffness and neutral angle defined by K_{max}, K_{min}, θ_{plant}, and θ_{dorsi} over reasonable stage dimensions h, H, and W (Appendix B). To visualize every possible solution and reduce computational time, a bounded-solution strategy was imposed to solve for sets of solutions in the $l_{min} - l_{max}$ space (Table 5).

To set up the bounds, a relationship between the desired stiffnesses and stage dimensions was derived using (7). From initial analysis, it was determined that the parameter b had little effect on the final solution, so $b = 4$ was chosen as it resulted in the simplest outcome to the integral, presented as (21).

$$K = -\frac{Erw^4\left(al_{eff} + 1\right)(r^3 - 4r^2 + 6r - 4)}{2l_{eff}} \tag{21}$$

Using the knowledge that l_{min} corresponds to the maximum stiffness and l_{max} corresponds to the minimum stiffness, (22) and (23) were derived. These relationships were used to generate bounds on the solution for the $l_{min} - l_{max}$ space (Figure 18, Table 5). Using those bounds, a solution region was identified and the desired values for E, l_{min}, and l_{max} were selected as free choices (Figure 19). From there, the remaining parameters for the stage and beam were calculated. While an infinite number of solutions exist, one particular solution with a HDPE beam ($l_{min} = 45mm, l_{max} = 195mm, E = 1.07GPa$) was chosen to use as a proof of concept for this design; its parameters are provided in Table 6.

$$a = -\frac{K_{max}l_{min} - K_{min}l_{max}}{l_{min}l_{max}(K_{max} - K_{min})} \tag{22}$$

$$E = \frac{-2l_{max}l_{min}(K_{max} - K_{min})}{w^4(l_{max} - l_{min})(r^4 - 4r^3 + 6r^2 - 4r)} \tag{23}$$

Table 5: Constraints imposed on the stage and beam design optimization.

	Constraint	Definition
-	Minimum Beam Width, w	$10mm = w_{min} \leq w$
-	Maximum Beam Width, w	$w \leq w_{max} = 20mm$
A	Minimum Young's Modulus, E_{min}	$0.3\ GPa = E_{min} \leq E$
B	Maximum Young's Modulus, E_{max}	$1.2\ GPa = E_{max} \geq E$
C	Maximum stage height, l_{max}	$l_{max} \leq 200\ mm$
D	Minimum Beam Thickness, t_{min}	$t \geq t_{min} = 1\ mm$
E	Moment of Inertia Curvature	$a < 0$
F	Minimum Stage Range	$H = l_{max} - l_{min} \geq 150\ mm$

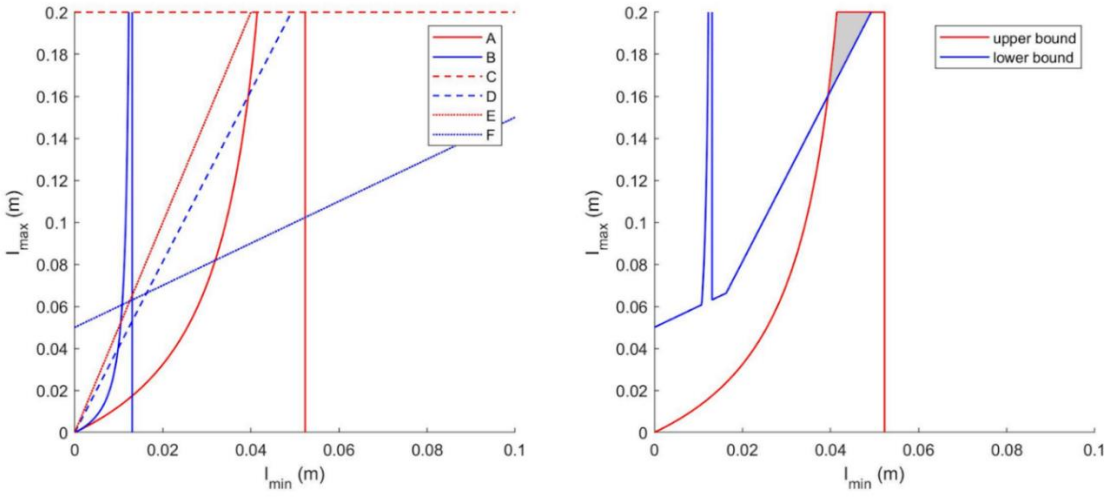

Figure 18: Bounds imposed on the solution plotted in the $l_{min} - l_{max}$ space.

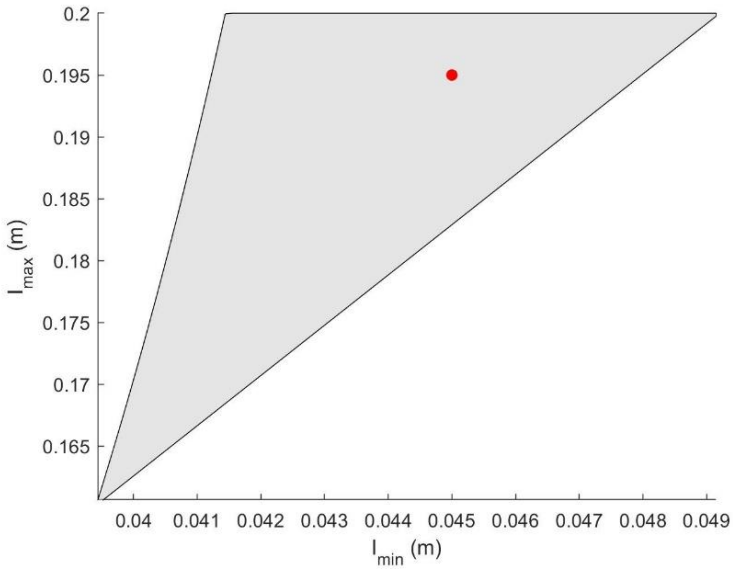

Figure 19: Solution space with solution selected for this project.

Table 6: Stage and beam properties determined using optimization.

E	1.07 GPa
l_{min}	45 mm
l_{max}	195 mm
θ_{range}	20 deg
t_0	12 mm
W	68.8 mm
w	15 mm

2.3.5 Concept Validation

For the variable cross-section beam derived, it can be shown that by varying the beam thickness, it is possible to achieve the desired stiffness range over a smaller stage size (Figure 20). The nonlinear beam moment of inertia also lends itself to a more linear stiffness-length profile, reducing the sensitivity of the beam stiffness to the beam length at high stiffnesses.

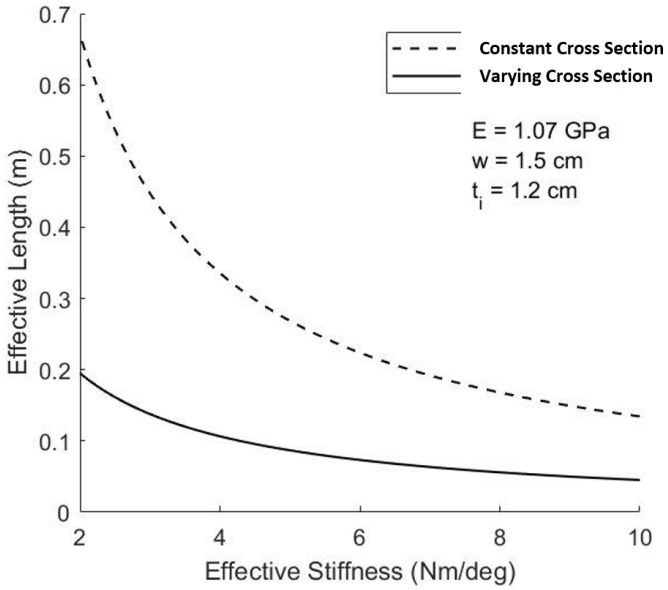

Figure 20: Length v. stiffness curves for beams with constant and variable cross-section profiles.

2.4 Transmission Design

Three concepts were considered to actuate the stage remotely from components worn at the hip. To avoid placing heavy motors at the ankle, three transmissions were considered, two involving fluid lines, and one involving cables (Figure 21). A fourth option involves placing lightweight motors at the ankle, though this was not investigated in detail. For this project, the hydraulic-based transmission concepts were explored in depth, and a pump-based transmission was determined to be the most feasible approach of the two as it allows for independent control of four piston-cylinders at the ankle using only one motor.

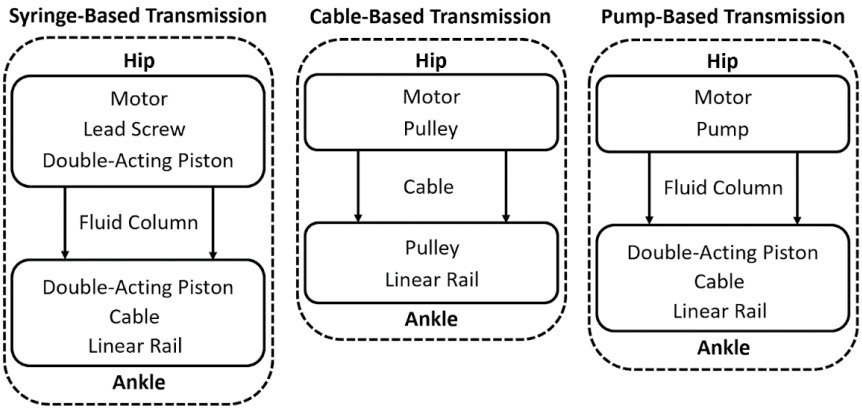

Figure 21: Transmission concepts considered for this project.

2.4.1 Cylinder Design

For either fluid-based transmission, custom hydraulic cylinders must be designed in order to actuate the stage at the ankle (Figure 22). These cylinders make up part of the weight of the ankle exoskeleton, so a minimalist design was required. For the cylinder material, 7075-T6 Aluminum was selected for its low density, manufacturability, and strength.

Figure 22: Rendered hydraulic cylinder for transmission.

A cylinder concept from the PHAFO project was adapted for this application. The piston in a double-acting cylinder is rigidly connected to a cable such that when the piston moves, the cable is pulled in either direction. By this, the piston motion can be transmitted to motion of an external body - in this case, the stage. Because the stage must have two degrees of freedom, two cylinders are required for stage motion, resulting in four cylinders total on the exoskeleton (Figure 23).

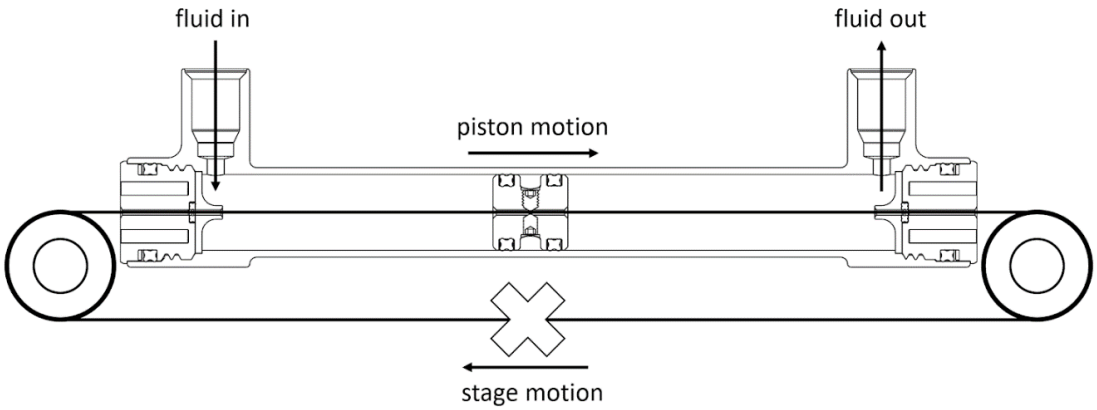

Figure 23: Hydraulic cylinder design and working principle.

The cylinder assembly is composed of three subassemblies: the piston, the cylinder, and the end caps (Figure 24). To ensure proper sealing and minimize leakage, quad ring seals were selected, and seal gusset dimensions were calculated by the standards provided by MN Rubber (Appendix E) [39]. For the conduits connecting the hip pack to the cylinders, hydraulic bicycle brake hose (Jagwire Pro Hydraulic Hose) was selected for its lightweight and minimal fittings. Weight was reduced by integrating a custom female connection for the hose fittings into the cylinder design, rather than relying on heavy stock hydraulic fittings (Appendix F).

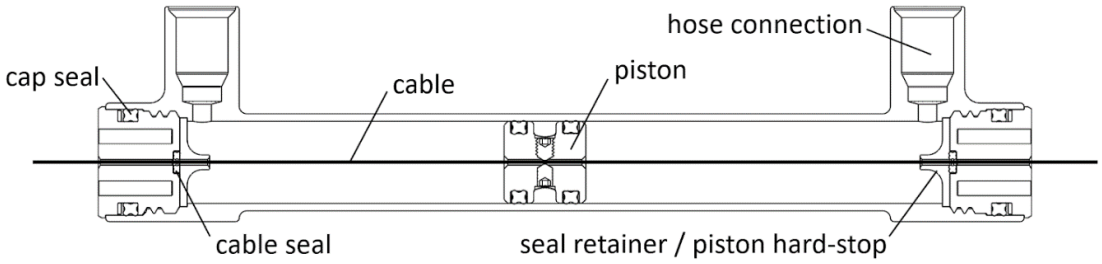

Figure 24: Component callout for custom hydraulic cylinder.

2.4.2 Hydraulic System Approaches

For the pump-based transmission system, four approaches to fluid control could be considered (Table 7).

Table 7: Combinations of hydraulic approaches to consider.

	Reversible Pump	**Irreversible Pump**
Four Valves	Assessed	Not Yet Assessed
Eight Valves	Not Yet Assessed	Not Yet Assessed

The first two approaches consist of a reversible pump at the hip, in series with a grouping of the four cylinders in parallel (Figure 25). In one scenario, a 2/2 valve is placed at one end of each cylinder to ‘lock’ each piston in place. To adjust the position of any stage, the corresponding valve can be opened, allowing the pump to move fluid from one chamber

of the cylinder to the other, thereby moving the piston. With this four-valve scenario, the pump must be capable of withstanding the system pressure generated by the forces on the piston as the patient walks. Alternatively, a second valve may be placed on the opposing side of each cylinder to cut off flow to the pump completely. With this, only the valves must be able to withstand the differential pressure of the system generated during walking. The weight and cost tradeoffs between an eight-valve, low pressure reversible pump system, and a four-valve, high pressure reversible pump system need to be evaluated. For this project, the four-valve, reversible pump system was evaluated.

Another option is to replace the reversible pump with an irreversible pump and 4/3 directional control valve (Figure 26). By doing so, more miniature pumps on the market may be considered. Such a configuration could again use either four or eight valves. The weight, space, and cost tradeoffs between the reversible-pump system and the control valve system need to be evaluated.

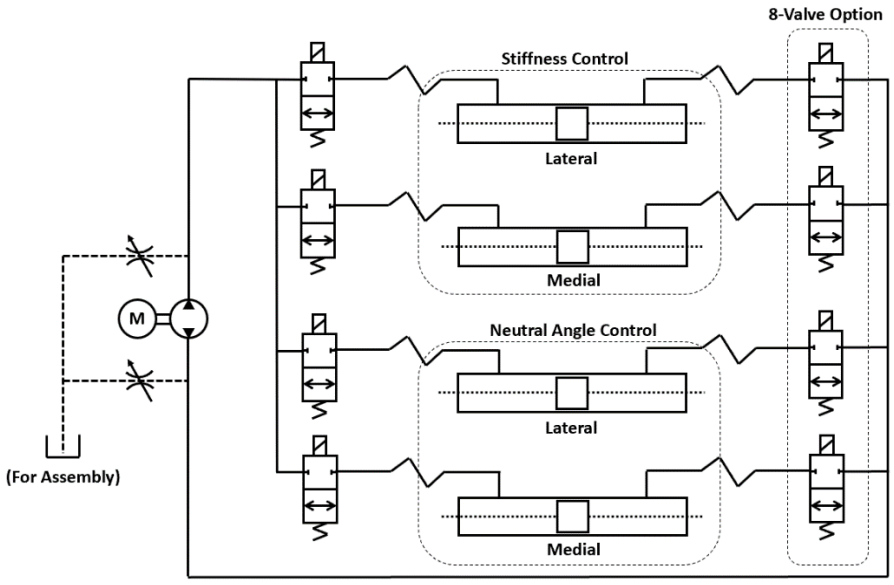

Figure 25: Hydraulic schematic for reversible pump circuit.

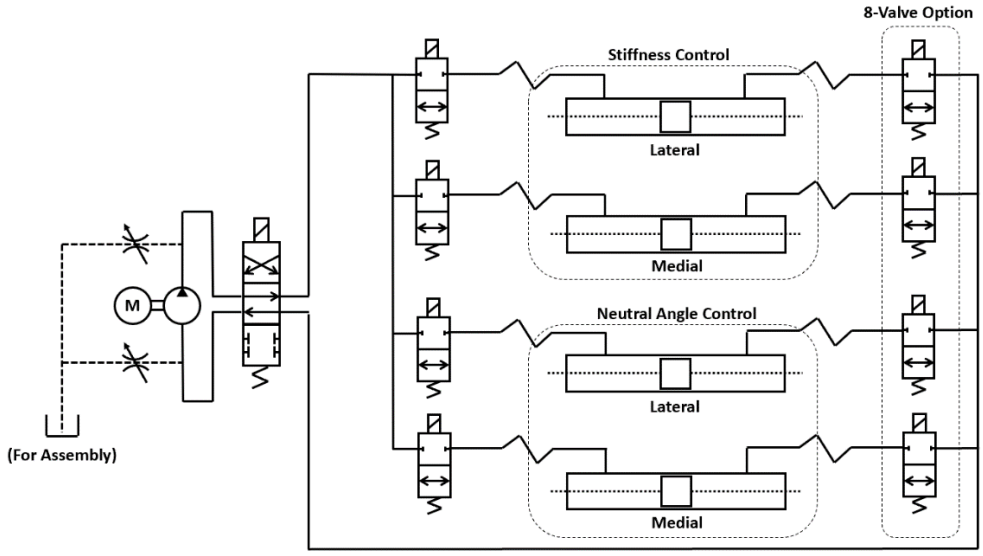

Figure 26: Hydraulic schematic for irreversible pump circuit.

2.4.3 System Specifications

For the stiffness and neutral angle to be adjusted at a reasonable speed, a constraint was placed on the minimum flow rate into each cylinder. A minimum piston speed of $v = 0.05\ m/s$ (to cover the full range of stiffnesses in 3 sec for a cylinder bore of $D = 11\ mm$) was selected using (24), the minimum flow rate going into each cylinder was calculated to be $Q = 0.53\ L/min$ (0.14 gpm). The cylinder bore was chosen from pressure analysis on the system. Because two cylinders are likely operated at the same time to control both the medial and lateral load positions, this flow rate is doubled to get the minimum flow rate required by the pump.

$$Q = A_{cylinder} v \tag{24}$$

To assess the expected pressures in the system, the circuit was simplified by assuming flow of mineral oil to only one cylinder (Figure 27). The simplified circuit can be characterized by pressure drops across the pump, valve, long conduits, and cylinder. Assuming a frictionless piston, P_3 and P_4 are equal. The pressure drop across the valve was estimated using the orifice equation (25), and the pressure loss in the conduits ($L = 1\ m$) was estimated using the Darcy-Weisbach equation (26). The pressure drop across the pump is just the sum of the pressure drops across each component.

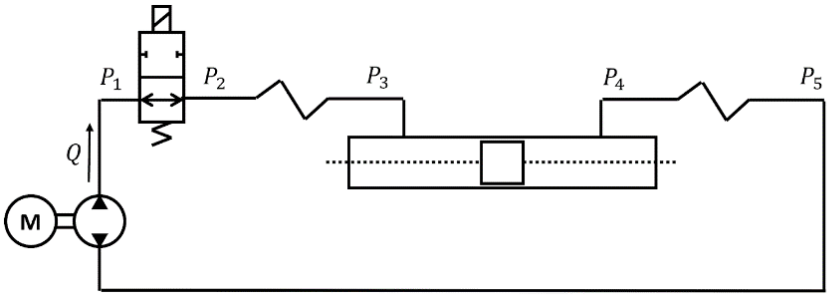

Figure 27: Description of hydraulic sub-circuit pressures.

$$Q = C_d A_{orifice} \sqrt{\frac{2\Delta P}{\rho}} \tag{25}$$

$$\frac{\Delta P}{L} = f_D \left(\frac{\rho}{2}\right)\left(\frac{v^2}{D}\right) \tag{26}$$

Table 8 provides the values used to calculate the pressure drop across each component. The pressure loss in the conduits was negligible. Results are provided in

Table 9. For higher flow rates, the pressure drop across the valve will increase, so this should be carefully considered if a larger flow rate is used in the system. As a safety precaution, a pressure relief valve should be included to protect the components.

Table 8: Values used in pressure analysis.

Q	0.28 gpm
f_D	0.00001
L	1 m
C_d	0.6
$D_{orifice}$	0.001
ρ	870 Kg/m^3

Table 9: Results of pressure analysis.

Pressure Drop Across Valves	88 psi
Pressure Drop Across Conduits	$4.2x10^{-7}$ psi
Pressure Drop Across Pump	88 psi

When all valves are closed, the cylinders are locked. Therefore, the pressure in the system increases as a result of tension on the piston due to beam loading. From the data collected by GCSH, it was found that 95% of the AFOs prescribed fall within a maximum torque range of $-66\ Nm$ (plantarflexion, PF) to $21\ Nm$ (dorsiflexion, DF). Using this knowledge and the relationship between pressure and force (27), the peak pressure generated in the cylinder due to walking was calculated for a range of cylinder diameters (Figure 28). It was determined that a cylinder bore of $1.1\ cm$ would be used to balance the weight requirements at the ankle with the pressure requirements of the system. Therefore, the pump should be selected to withstand approximately $1000\ psi$ of burst pressure before a safety factor is applied for this circuit configuration. The component specifications for the four-valve, reversible pump circuit are summarized in Table 10.

$$f = PA_{cylinder} \tag{27}$$

Table 10: Required pressure and flow specifications for pump and valves.

	2/2 Valves	**Pump**
Minimum Flow Rate	–	$0.28\ gpm$
Burst Pressure	–	$1000\ psi$
Differential Pressure	$88\ psi$	$88\ psi$

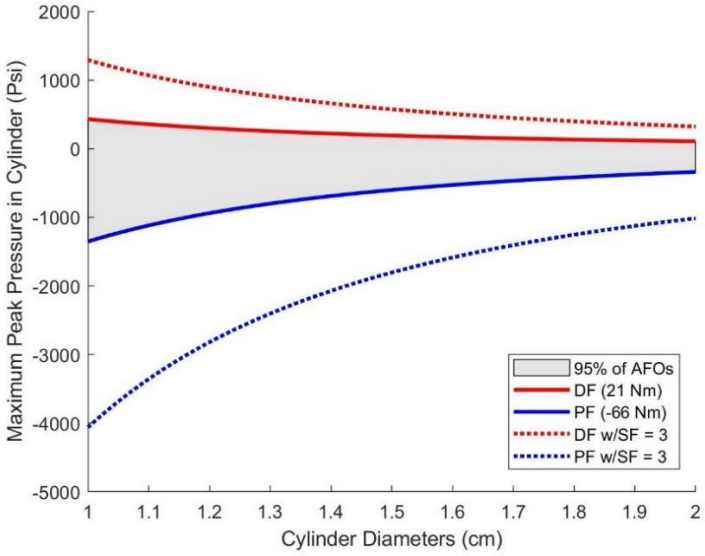

Figure 28: Peak pressures in cylinders of varying bore diameter.

2.4.4 Component Selection

To estimate the weight of the system worn at the hip, a reversible fixed-displacement miniature pump and solenoid valves meeting the requirements were selected; however, testing of these components was out of the project scope. Details for these components are summarized in Table 11, and their data sheets can be found in Appendix D.

Table 11: Pump and valves selected for hydraulic circuit.

	Description	Company	Model Number	Mass
Pump	Fixed displacement micro-pump	Hydro Leduc	PB32	0.33 Kg
Valves	2-way solenoid valve	The Lee Company	SDBB3321003A	0.07 Kg

2.5 Ankle Exoskeleton Design

The ankle exoskeleton is composed of a flexible foot plate used to mimic the spring behavior of an AFO, an adjustable beam mount that fixes the beams to the foot plate, two beams, and a mounting structure to attach the stage to the limb (Figure 29). The designs presented were derived for the purpose of establishing a base concept and weight estimate of the device, so minor adjustments may need to be made in the future.

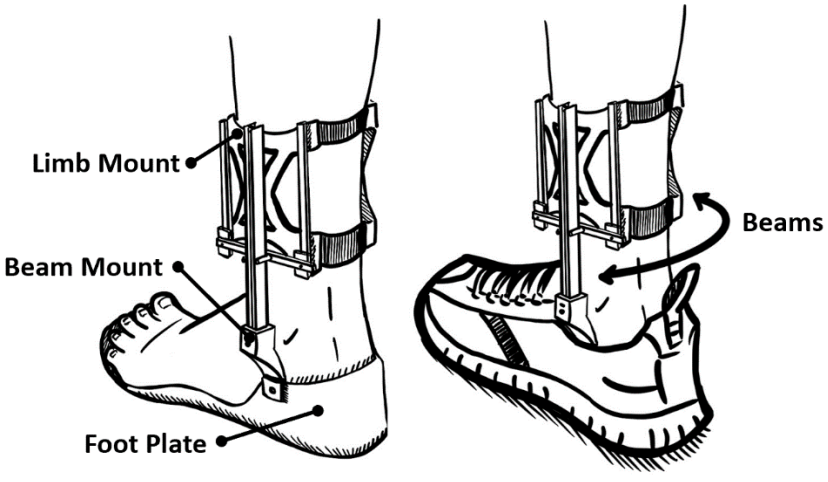

Figure 29: Concept art of exoskeleton with component callouts.

2.5.1 Limb Mount

The purpose of the limb mount is to hold the stage components in place at the ankle. A methodical approach to the design was taken to minimize the weight at the ankle; however, this structure was primarily designed for the purposes of demonstrating the concept and was not evaluated as minimum weight.

Functional components (cylinders, linear rails, and cable guides) were first placed in the modeling software. The stage structure was then modeled around the necessary components to achieve the minimum structural integrity required and to accommodate the shape of the lower leg. It was important to design the limb mount such that the beams did not protrude from the limb and risk the medial beam hitting the patient's other leg as they walked. A cable-pulley system was designed to transmit the motion of the hydraulic pistons to the motion of the load point on the stage in either the vertical or horizontal direction, though the cable itself was omitted from the model for simplicity. The structures loading the beam, holding the pulleys in place, and connecting the cable to the stage were also modeled around each component. The limb will be printed in polycarbonate to balance strength and lightness.

2.5.2 Beam

The I-beam with varying thickness was modeled in CAD to later assess the device stiffness using FEA and estimate the final weight at the ankle (Figure 30). HDPE was applied as the material.

Figure 30: Side (right) and top (left) views of the beam.

2.5.3 Beam Mount & Foot Plate

To accommodate a wide range of patient foot sizes, it was important that the beam mounting structure be adaptable to different foot plate shapes and dimensions. Likewise, it was important to design a footplate that could easily be manufactured for a wide variety of feet while maintaining a standard connection to the beam mount. For this project, a solid model of a leg was referenced to generate the foot plate using surface modeling techniques (Figure 31). Once a natural shape was established, the heel was modified to meet up with a standardized elliptical body that matched the dimensions of the beam mount. A thin extrusion from the elliptical shape was added, with the intention of acting as a Velcro joint to fix the beam mount to the foot plate. The foot plate should be constructed from LDPE.

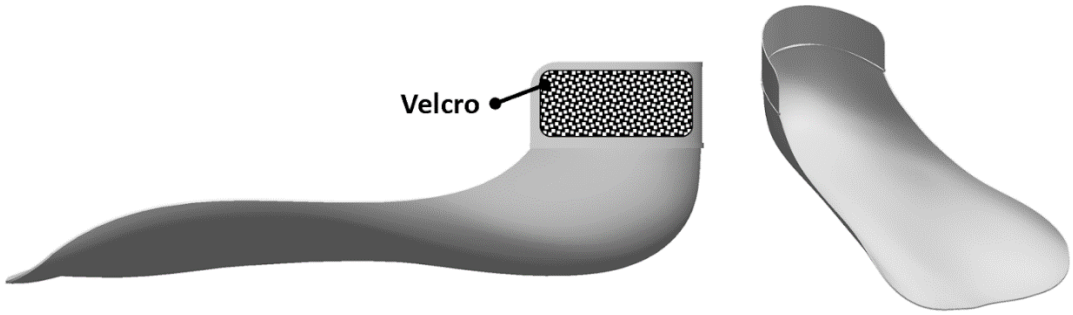

Figure 31: Model of the foot plate.

The purpose of the beam mount is to fix both beams to the foot plate. Therefore, the mount must be structural rigid and capable of withstanding the loading on the beam. To design the beam mount for minimal weight, a topology study was performed with the goal of reducing the part material just enough to achieve the best stiffness to weight ratio. First, a base solid was generated to establish the slots for each beam and the joint connecting the mount to the foot plate (Figure 32).

Using the expected maximum forces on each beam (force of $733\ N$ acting at the minimum beam length of $45\ mm$ resulting in a total of $66\ Nm$ of PF torque) and an applied safety factor of 1.5, the forces within the beam mount were estimated with a simplified lever model and applied to the body for the optimization (Figure 33). Polycarbonate was selected as the material for its printability, strength, and low density. The resulting mass-optimized

model was then exported as a graphics object and referenced to generate the final refined structure for the beam mount (Figure 34).

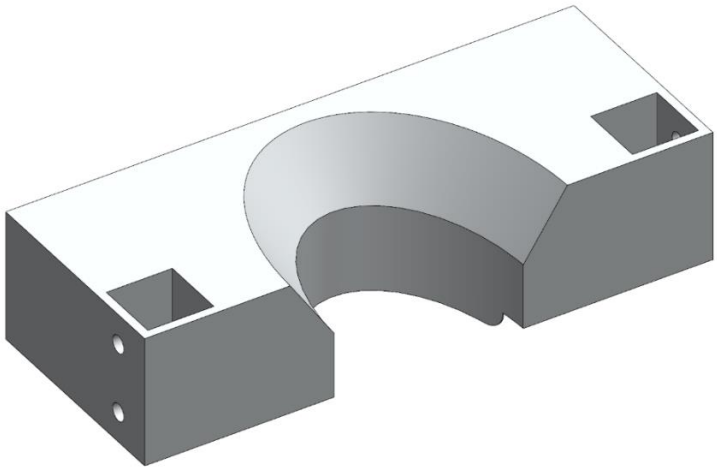

Figure 32: Base solid of beam mount used for topology optimization.

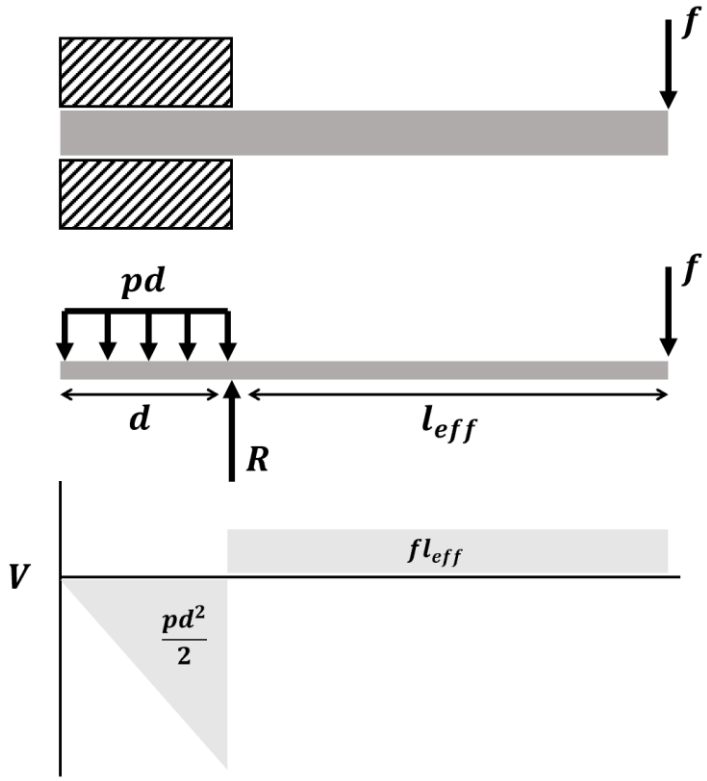

Figure 33: Lever simplification used to solve for forces in beam mount.

Figure 34: Topology optimization results (top) and resulting model of beam mount (bottom).

2.6 Total Device Stiffness

To calculate the stiffness range of the device, the compliance in all components must be considered. In doing so, the stiffness range defined by the beam design will be reduced; however, higher stiffness may yet be achieved by calibrating the device. The base stiffness as defined by the beam optimization is a function of the total deflection on the beam at the load point. Additional compliance in the hydraulic oil of the cylinders and the beam mount (the cable and limb mount are assumed to be rigid) must be subtracted from the total deflection of the beam to determine the actual stiffness of the device (27).

$$K_{actual} = \frac{2fl_{eff}^2}{\delta - \Delta x_{cyl} - \Delta x_{mount}} \tag{27}$$

Deflection of the beam mount must be determined using simulation. However, the compliance of the hydraulic fluid can be computed analytically using the Cho model, which estimates the bulk modulus of a fluid with entrained air (28) [40]. To do so, the hydraulic cylinder restricting motion along the horizontal (the cylinder controlling the neutral angle) can be approximated as a spring with force f acting on the compressed fluid volume in the cylinder (Figure 35). The initial fluid pressure, P, can be approximated as zero; using the relationship between pressure, volume, and bulk modulus, the relationship between the force on the cylinder and the ratio of the initial piston position over its deflection is derived (29). By combining the equation for the device stiffness (27) with (29), the definition for the actual device stiffness as a function of the neutral angle piston position, x, was derived (30). This expression can be written as a relationship between the desired stiffness, K_{des} and the actual device stiffness K_{actual} (31). To evaluate, x may be written as a ratio r of the cylinder length W, which can later be used as a parameter for the neutral angle (32).

$$\beta_e = -V\left(\frac{\Delta \mathrm{P}}{\Delta \mathrm{V}}\right) = \beta\left\{\frac{R + \left(\frac{P}{P_{atm}} + 1\right)^{\frac{1}{\gamma}} e^{-\frac{P}{\beta}}}{\frac{R}{\gamma}\left(\frac{\beta}{P + P_{atm}}\right) + \left(\frac{P}{P_{atm}} + 1\right)^{\frac{1}{\gamma}} e^{-\frac{P}{\beta}}}\right\} \tag{28}$$

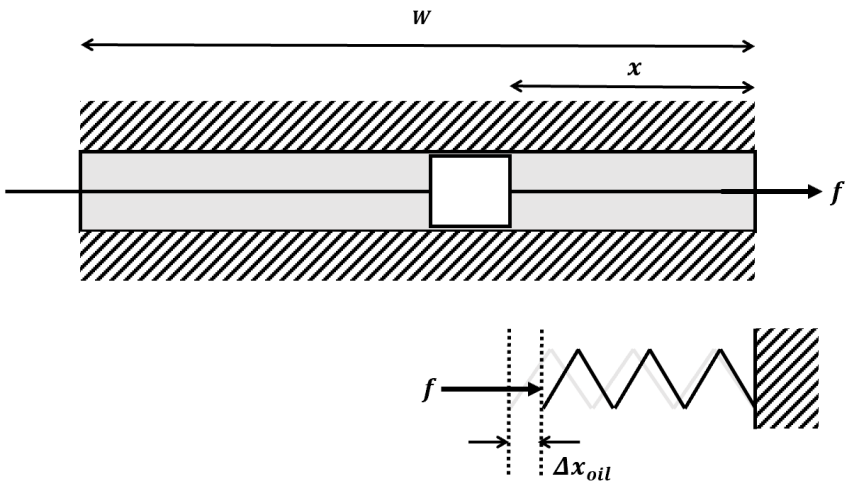

Figure 35: Spring simplification of compressed fluid in hydraulic cylinder.

$$\frac{x}{\Delta x} = -\frac{\beta A}{f}\left\{\frac{R+1}{\frac{R}{\gamma}\left(\frac{\beta}{P_{atm}}\right)+1}\right\} = \frac{C}{f} \tag{29}$$

$$K_{actual} = \frac{2l_{eff}}{\frac{2l_{eff}}{K_{des}} - \frac{x}{l_{eff}C} - \frac{\Delta x_{mount}}{T_{ankle}}} \tag{30}$$

$$\frac{1}{K_{des}} - \frac{1}{K_{actual}} = \frac{x + \frac{\Delta x_{mount}}{T_{ankle}} l_{eff}C}{2l_{eff}^2 C} \tag{31}$$

$$x = rW \tag{32}$$

3 Methods for Design Evaluation

3.1 Weight Evaluation

Each component of the exoskeleton was modeled and assigned material properties in SolidWorks to estimate the total weight of the device at the ankle. Custom components such as the limb mount, beam mount, and foot plate were designed to be lightweight. In particular, the beam mount was designed to be minimum weight using topology optimization. To verify that the beam mount is designed at a minimum weight with

maximum stiffness, an assembly of the beam mount and two beams was loaded under the maximum expected force conditions and the stresses in the part were observed.

3.2 Stiffness Evaluation

The beam stiffness model can be verified by performing a deflection analysis for various forces on the beam. Six loading conditions were applied to the fixed beam in an FEA simulation and the deflection along the beam was measured. Simulation results were then plotted against the expected analytical values for comparison. To compare the torque-angle and hysteresis properties of the beam with that of the traditional AFO, the model was subjected to sinusoidal loading in an FEA program and deflection data was collected at the load point.

The total device stiffness in the PF and DF states can be measured by finding the deflection of the beam mount under the maximum torque loading condition and applying (30). This was done using a static simulation on the model.

4 Results

4.1 Beam Mount Stress Analysis

A static stress simulation at the maximum PF and DF loading conditions was performed on the beam mount. Results indicate that there were no regions of peak stress in the mount and that the stresses were reasonably dispersed over the structural members. Still, many areas showed little stress and may indicate that more material could be removed to achieve minimum weight.

4.2 Weight Assessment

Material properties were assigned to each component in the model, and a mass estimate was gathered for each. The assembly can be broken into subcategories representing the main weight groups for the design (Figure 36). These subcategories may also be classified as either part of the base exoskeleton (the structure solely responsible for the stage) or the hydraulic-based transmission. By dividing the assembly this way, it was possible to

evaluate the effectiveness of the hydraulic transmission at minimizing the weight of the device, as well as see which parts of the assembly are contributing the most to the total mass.

The base exoskeleton was estimated to weigh approximately 215 g, which is below the design requirement of 237 g. With the addition of the hydraulic transmission, the total weight of the device is 425 g, which is 210 g over the target weight, 25 g heavier than the heaviest AFO weighed at GCSH, and about 65% lighter than both the HAFO and the EXO-001 by Humotech without a shoe (Figure 37).

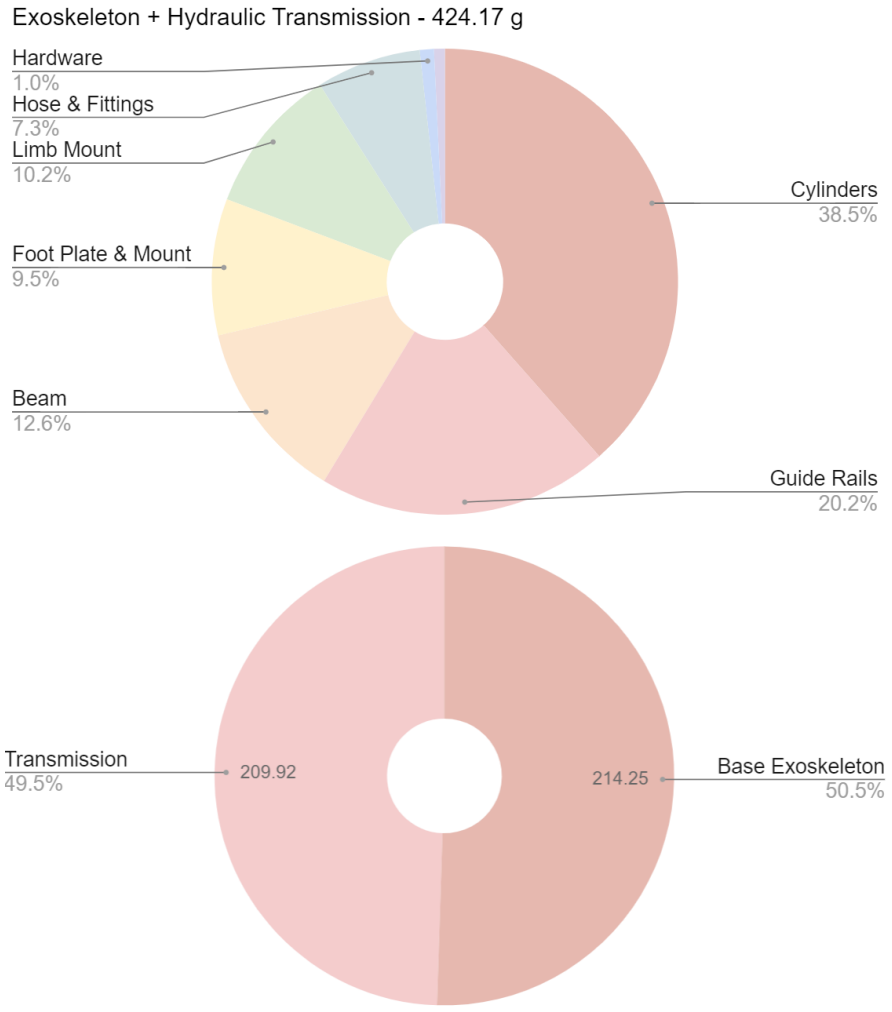

Figure 36: Mass breakdown of the Autotuner exoskeleton.

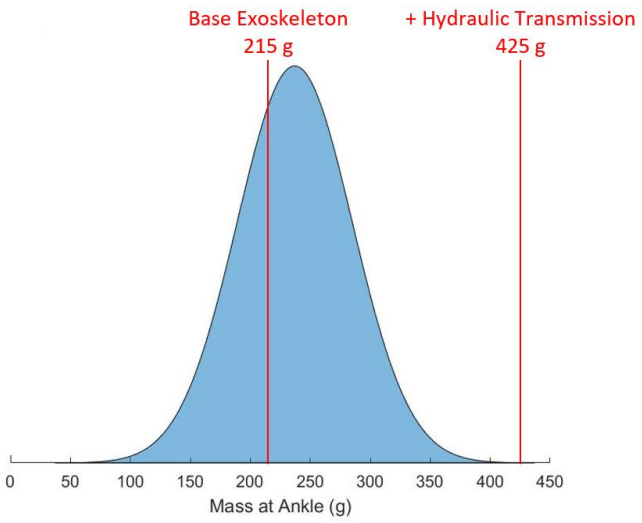

Figure 37: Comparison of Autotuner mass with AFOs prescribed at GCSH.

4.3 Stiffness Assessment

4.3.1 Beam Verification

To verify that the analytical beam solution is a good representation of a physical model, a deflection assessment on the beam was performed. The beam was first modeled before material properties were applied for HDPE and the beam was subjected to a load of 100 N at six different locations relating to six different stiffnesses (Table 12). Data was generated for the deflection of the beam from the base to the end and then fit with a polynomial in order to estimate the deflection at the load position. The effective stiffness was then computed for each of the six simulations and compared with the analytical solution (Figure 38).

Table 12: Stiffness values tested in ANSYS beam assessment.

Effective Length (m)	Expected Stiffness (Nm/deg)
0.0450	10.00
0.0556	8.02
0.0723	6.08
0.1071	3.97
0.1374	3.01
0.1950	2.00

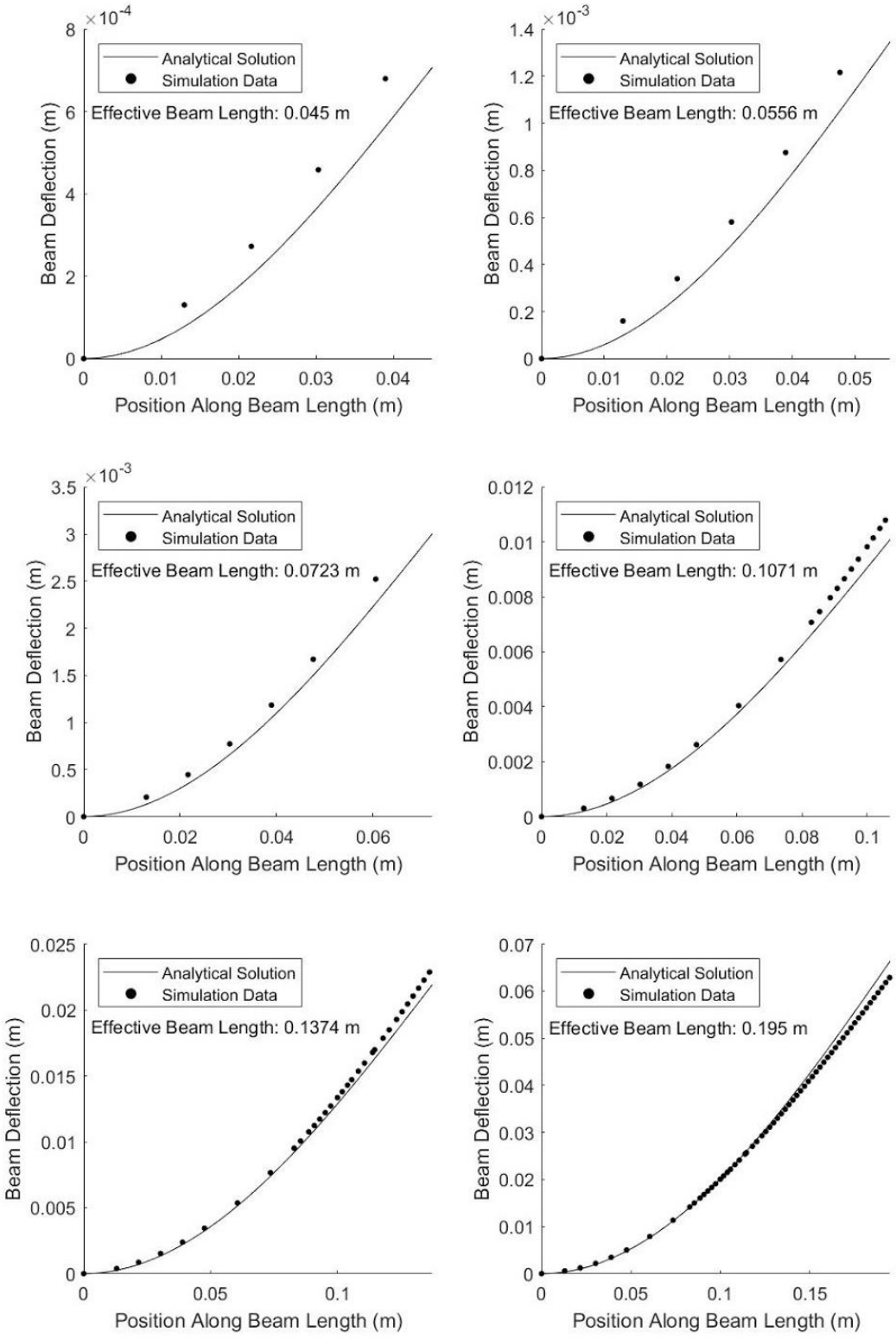

Figure 38: ANSYS deflection results plotted against analytical solutions.

It can be seen from Figure 39 that the difference between the analytical model and the physical simulation is greater at the stiffer beam settings. This is consistent with the slender beam assumption. Additional error can be attributed to assumptions made in modeling such as the small angle assumption, as well as imperfect solid modeling of the beam and numerical error. While this error impacts the overall stiffness profile of the physical beam, this error was anticipated and should be combated by calibrating the device using BRUCE prior to each use.

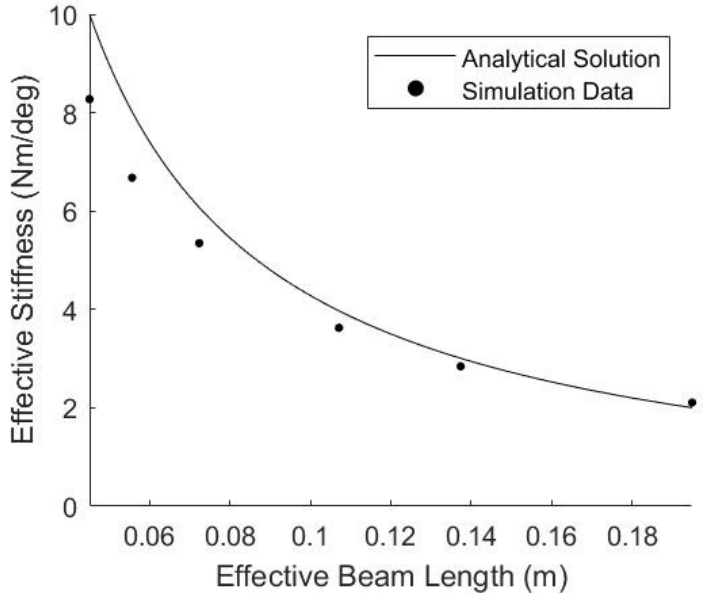

Figure 39: Stiffness v. beam length for analytical solution and ANSYS data.

4.3.2 Total Device Stiffness

The deflection of the beam mount under the maximum loading conditions (PF & DF) was measured using FEA to find an approximation for $\Delta x_{mount}/T_{ankle}$. A deflection of $0.95\ mm$ under $66\ Nm$ PF torque and a deflection of $3.36\ mm$ under $21\ Nm$ DF torque were measured. These values and the results from the beam stiffness assessment were applied to (30) to observe the impact of the neutral angle position on the device stiffness (Figure 40). The total device stiffness curve was then computed using (29) and compared with the analytical solution (Figure 41).

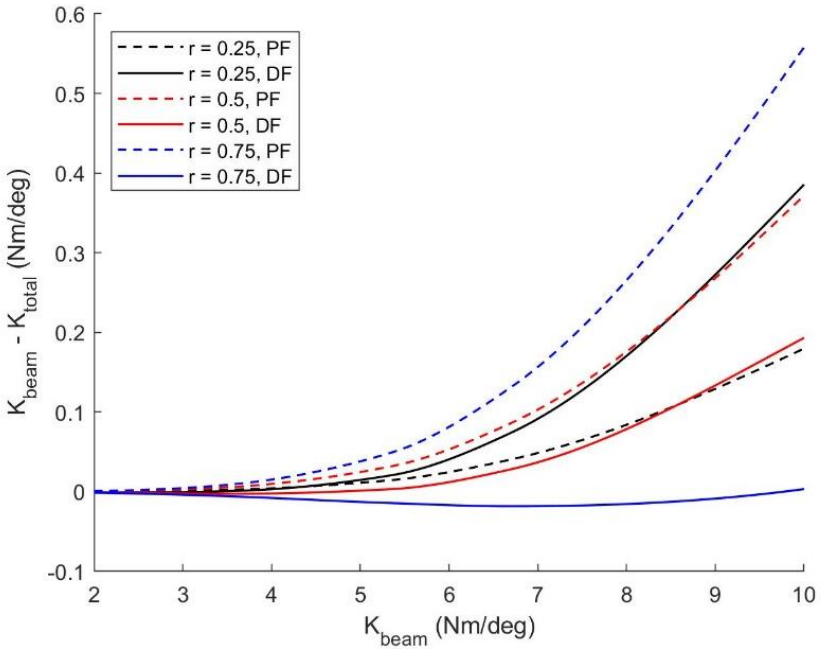

Figure 40: Difference between beam stiffness and total device stiffness for varying r.

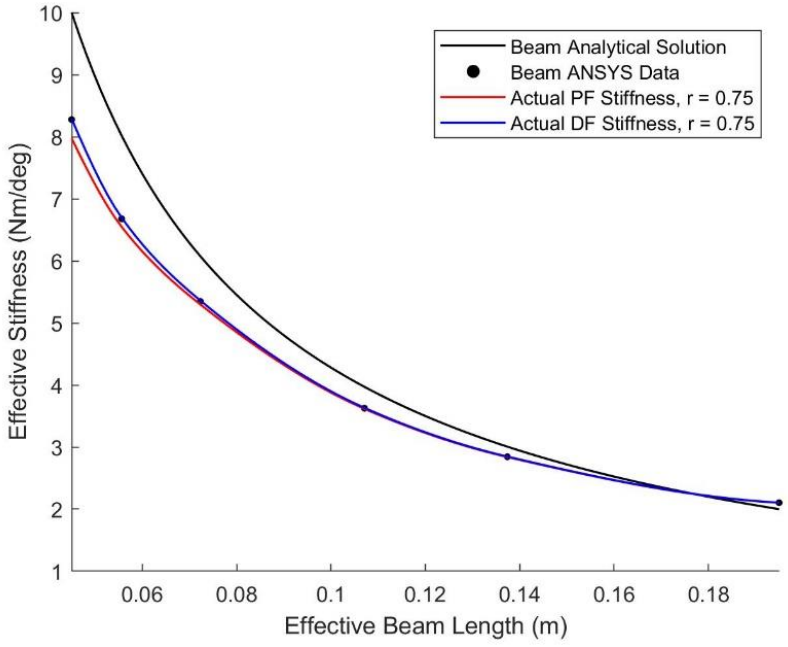

Figure 41: Analytical and total device stiffness curves in the PF and DF directions.

4.4 AFO Performance Comparison

To compare the loading behavior of the variable thickness I-beam with a traditional AFO, the beam model was subjected to sinusoidal loading at the effective beam length resulting in a stiffness of 2 Nm/deg using FEA software and its deflection was measured. This was plotted against data collected at GCSH using BRUCE on an AFO with the same stiffness (Figure 42). The beam simulation produced linear torque-angle data compared to the AFO stiffness - this was anticipated as the physical methods used to test the AFO with BRUCE could not be replicated virtually.

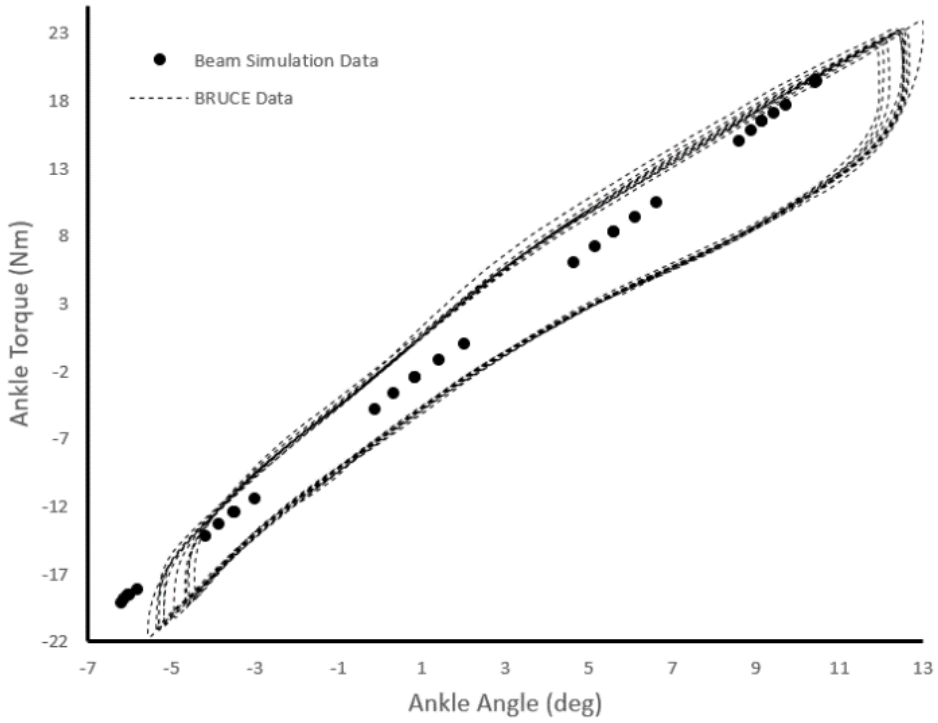

Figure 42: ANSYS results from cyclic loading on beam.

5 Discussion

5.1 Design Requirements

The proposed concept met neutral angle and size design requirements but falls short of the stiffness and weight requirements (Table 13). The stiffness range generated with the optimization was 2 Nm/deg to 10 Nm/deg; however, the simulation results showed that the range was smaller (2 Nm/deg to 8 Nm/deg). To achieve stiffnesses below 2 Nm/deg, the beam was lengthened with a constant cross section at the end. Calibration of the device would be necessary to account for patient fit differences, so calibrating the device to the full range of stiffnesses should be possible. It is suggested that beams with different stiffness ranges be designed based on the patient's weight to maximize the overall stiffness resolution of the device; for instance, a smaller beam could be designed for a stiffness range covering 0.5 Nm/deg to 5 Nm/deg and used for children who need a more flexible AFO. The stiffness does not consider compliance of the limb or foot plate, which are both rigidly fixed when a device is measured with BRUCE. The neutral angle range is only dependent on the width of the stage and the horizontal position of the stage relative to the vertical beam. A 20 deg range (approximately 7 cm stage width) was easily achieved without the device becoming overly large. The device dimensions were optimized to meet the size requirements, with the height of the Autotuner being approximately 21 cm. It is proposed that sensors be placed at the stage to provide positional feedback to the controller in order to minimize stiffness and angle error over time.

It was demonstrated that the base exoskeleton is within the normal mass range of AFOs prescribed at GCSH and that the full exoskeleton is equivalent in mass to the heaviest AFOs. A 65% weight reduction compared to the HAFO and EXO-001 is significant and demonstrates the validity of this approach for a lightweight exoskeleton.

Table 13: Design requirement verification.

Requirement	Target Value	Actual Value
Stiffness Range	1 Nm/deg to 10 Nm/deg	2 Nm/deg to 8 Nm/deg
Neutral Angle Range	20 deg	20 deg
Weight at Ankle	237 g	424.9 g
AFO Height	< 31 cm	21 cm

5.2 Design Limitations

The major limitation of this design is that a physical prototype has yet to be created and tested. There will inevitably be ergonomic challenges with mounting the limb to the device that cannot be solved without a physical model. One challenge will be keeping the stage from sliding on the patient's lower limb. A potential solution would be to use medical grade tape to hold the stage in place.

A second foreseen challenge is out-of-plane bending and twisting of the beams as the patient walks. One addition to consider for the exoskeleton would be a rigid wall on the outermost edge of the beams, like an acrylic cover, to constrain the beams to in-plane bending only.

The uniqueness of the structural shapes proposed with this design opens the door for manufacturing challenges. Structural components such as the stage mounting system could be 3D printed, and even adjusted to accommodate the patient's size if necessary. However, the beams would need to be either cast or milled from stock HDPE, and the variable beam thickness might be difficult to obtain.

5.3 Alternative Directions

Other methods for varying the stiffness of the ankle joint were considered. Rather than using a horizontal stage to change the neutral angle, a physical rotation of the beam base using a worm gear and motor system was considered. This would reduce the overall width of the device by removing the need for a wide stage; it would likely require a motor at the ankle heavier than the rail and cylinder system, though the concept holds potential. Torsional springs systems were also considered, but ultimately a beam-based design was selected as it does not constrain the ankle rotation about a fixed pin joint. One concept that was imagined later in the design process is the inverse of the idea proposed in this paper: rather than the beam being flexible and the load point rigid, the beam could be rigid and the load point could vary in compliance either by using a coil or air spring system. This idea could eliminate the need for the vertical stage and would likely reduce the overall weight at the ankle.

5.4 Future Work

The next steps in the design process would be to develop a test bench for the hydraulic transmission using the custom cylinders and bicycle hose. It would be ideal to also create a prototype of the beam for physical testing with the transmission. From there, an optimal layout for the hip pack should be developed, and a controller should be designed and tested. The exoskeleton mounting the components should be revisited in detail before the final product is developed to ensure structural integrity and ergonomics.

References

[1] CDC, “Learn More About Cerebral Palsy (CP) | CDC,” *Centers for Disease Control and Prevention*, Mar. 02, 2020. https://www.cdc.gov/ncbddd/cp/index.html (accessed Jul. 15, 2020).

[2] *Capute & Accardo’s neurodevelopmental disabilities in infancy and childhood*, 3rd ed.. Baltimore: Paul H. Brookes Pub., 2008.

[3] D. Christensen *et al.*, “Prevalence of cerebral palsy, co-occurring autism spectrum disorders, and motor functioning – Autism and Developmental Disabilities Monitoring Network, USA, 2008,” *Dev. Med. Child Neurol.*, vol. 56, no. 1, pp. 59–65, 2014.

[4] C. L. Arneson *et al.*, “Prevalence of cerebral palsy: Autism and Developmental Disabilities Monitoring Network, three sites, United States, 2004 †,” *Disabil. Health J.*, vol. 2, no. 1, pp. 45–48, 2009.

[5] C. Morris, “Orthotic Management of Children with Cerebral Palsy,” *JPO J. Prosthet. Orthot.*, vol. 14, no. 4, pp. 150–158, 2002.

[6] D. K. Walker, J. S. Palfrey, J. A. Butler, and J. Singer, “Use and Sources of Payment for Health and Community Services for Children with Impaired Mobility,” *Public Health Rep. 1974-*, vol. 103, no. 4, pp. 411–415, 1988.

[7] M. Wingstrand, G. Hägglund, and E. Rodby-Bousquet, “Ankle-foot orthoses in children with cerebral palsy: a cross sectional population based study of 2200 children,” *BMC Musculoskelet. Disord.*, vol. 15, no. 1, p. 327, 2014.

[8] E. Figueiredo Mello, G. Ferreira Bastos, R. Maia Moreira César, R. Kirkwood Noce, and L. Fetters Noce, “Efficacy of Ankle-Foot Orthoses on Gait of Children with Cerebral Palsy: Systematic Review of Literature,” *Pediatr. Phys. Ther.*, vol. 20, no. 3, pp. 207–223, 2008.

[9] C. Morris, “A review of the efficacy of lower-limb orthoses used for cerebral palsy,” *Dev. Med. Child Neurol.*, vol. 44, no. 3, pp. 205–211, 2002.

[10] M. A. Brehm, J. Harlaar, and M. Schwartz, “Effect of ankle-foot orthoses on walking efficiency and gait in children with cerebral palsy,” *J. Rehabil. Med.*, vol. 40, no. 7, pp. 529–534, 2008.

[11] A. J. Ries, A. Rozumalski, and M. H. Schwartz, “Do ankle-foot orthoses improve gait for individuals with cerebral palsy?,” *Gait Posture*, vol. 38, pp. S20–S21, 2013.

[12] W. K. Lam, J. C. Y. Leong, Y. H. Li, Y. Hu, and W. W. Lu, “Biomechanical and electromyographic evaluation of ankle foot orthosis and dynamic ankle foot orthosis in spastic cerebral palsy,” *Gait Posture*, vol. 22, no. 3, pp. 189–197, 2005.

[13] A. J. Ries and M. H. Schwartz, “Ground reaction and solid ankle-foot orthoses are equivalent for the correction of crouch gait in children with cerebral palsy,” *Dev. Med. Child Neurol.*, vol. 61, no. 2, p. 219, 2019.

[14] D. Totah, M. Menon, C. Jones-Hershinow, K. Barton, and D. H. Gates, “The impact of ankle-foot orthosis stiffness on gait: A systematic literature review,” *Gait Posture*, vol. 69, pp. 101–111, 2019.

[15] N. Eddison and N. Chockalingam, “The effect of tuning ankle foot orthoses–footwear combination on the gait parameters of children with cerebral palsy,” *Prosthet. Orthot. Int.*, vol. 37, no. 2, pp. 95–107, 2013.

[16] D. J. J. Bregman, A. Rozumalski, D. Koops, V. de Groot, M. Schwartz, and J. Harlaar, “A new method for evaluating ankle foot orthosis characteristics: BRUCE,” *Gait Posture*, vol. 30, no. 2, pp. 144–149, 2009.

[17] T. Kobayashi, A. Leung, Y. Akazawa, and S. Hutchins, “Design of a stiffness-adjustable ankle-foot orthosis and its effect on ankle joint kinematics in patients with stroke,” *Gait Posture*, vol. 33, no. 4, pp. 721–723, 2011.

[18] E. Russell Esposito, R. Blanck, N. Harper, J. Hsu, and J. Wilken, “How Does Ankle-foot Orthosis Stiffness Affect Gait in Patients With Lower Limb Salvage?,” *Clin. Orthop. Relat. Res.*, vol. 472, no. 10, pp. 3026–3035, 2014.

[19] W. K. Durfee, “Tuning Mechanical Properties of the Ankle Foot Orthoses Used by Children With Cerebral Palsy,” University of Minnesota, Gillette Children’s Specialty Healthcare, Proposal, Feb. 2020.

[20] A. J. Ries, T. F. Novacheck, and M. H. Schwartz, “A data driven model for optimal orthosis selection in children with cerebral palsy,” *Gait Posture*, vol. 40, no. 4, pp. 539–544, 2014.

[21] J. Davids R., F. Rowan B., and R. Davis B., “Indications for Orthoses to Improve Gait in Children With Cerebral Palsy,” *J. Am. Acad. Orthop. Surg.*, vol. 15, no. 3, pp. 178–188, 2007.

[22] K. J. Kane, J. L. Lanovaz, and K. E. Musselman, “Physical Therapists’ Use of Evaluation Measures to Inform the Prescription of Ankle-Foot Orthoses for Children with Cerebral Palsy,” *Phys. Occup. Ther. Pediatr.*, vol. 39, no. 3, pp. 237–253, 2019.

[23] K. Kane, P. Manns, J. Lanovaz, and K. Musselman, “Clinician perspectives and experiences in the prescription of ankle-foot orthoses for children with cerebral palsy,” *Physiother. Theory Pract.*, vol. 35, no. 2, pp. 148–156, Feb. 2019, doi: 10.1080/09593985.2018.1441346.

[24] A. Roberts, J. Wales, H. Smith, C. J. Sampson, P. Jones, and M. James, “A randomised controlled trial of laser scanning and casting for the construction of ankle–foot orthoses,” *Prosthet. Orthot. Int.*, vol. 40, no. 2, pp. 253–261, 2016.

[25] E. S. Schrank, L. Hitch, K. Wallace, R. Moore, and S. J. Stanhope, “Assessment of a virtual functional prototyping process for the rapid manufacture of passive-dynamic ankle-foot orthoses,” *J. Biomech. Eng.*, vol. 135, no. 10, pp. 101011–101017, Oct. 2013, doi: 10.1115/1.4024825.

[26] “The influence of ankle-foot orthosis stiffness on walking performance in individuals with lower-limb impairments- ClinicalKey.” https://www-clinicalkey-com.ezp1.lib.umn.edu/#!/content/playContent/1-s2.0-S0268003314001739?returnurl=null&referrer=null (accessed Jul. 20, 2020).

[27] T. Kobayashi, A. Leung, and S. Hutchins, “Techniques to measure rigidity of ankle-foot orthosis: A review,” *J. Rehabil. Res. Dev.*, vol. 48, no. 5, pp. 565–576, 2011.

[28] D. J. J. Bregman, A. Rozumalski, D. Koops, V. de Groot, M. Schwartz, and J. Harlaar, “A new method for evaluating ankle foot orthosis characteristics: BRUCE,” *Gait Posture*, vol. 30, no. 2, pp. 144–149, 2009.

[29] A. Oymagil, J. Hitt, T. Sugar, and J. Fleeger, “Control of a Regenerative Braking Powered Ankle Foot Orthosis,” Jul. 2007, pp. 28–34, doi: 10.1109/ICORR.2007.4428402.

[30] J. Ward, T. Sugar, A. Boehler, J. Standeven, and J. R. Engsberg, “Stroke Survivors’ Gait Adaptations to a Powered Ankle Foot Orthosis,” *Adv. Robot. Int. J. Robot. Soc. Jpn.*, vol. 25, no. 15, pp. 1879–1901, Jan. 2011, doi: 10.1163/016918611X588907.

[31] V. Arnez-Paniagua, H. Rifai, Y. Amirat, and S. Mohammed, “Adaptive control of an actuated-ankle-foot-orthosis,” in *2017 International Conference on Rehabilitation Robotics (ICORR)*, 2017, vol. 2017, pp. 1584–1589.

[32] J. Blaya and H. Herr, “Adaptive control of a variable-impedance ankle-foot orthosis to assist drop-foot gait,” *IEEE Trans. Neural Syst. Rehabil. Eng.*, vol. 12, no. 1, 2004, [Online]. Available: http://search.proquest.com/docview/883034473/.

[33] K. A. Shorter, G. F. Kogler, E. Loth, W. K. Durfee, and E. T. Hsiao-Wecksler, “A portable powered ankle-foot orthosis for rehabilitation,” *J. Rehabil. Res. Dev.*, vol. 48, no. 4, p. 459, 2011, doi: 10.1682/JRRD.2010.04.0054.

[34] Y. Bai, F. Li, J. Zhao, J. Li, F. Jin, and X. Gao, “A powered ankle-foot orthoses for ankle rehabilitation,” in *2012 IEEE International Conference on Automation and Logistics*, Aug. 2012, pp. 288–293, doi: 10.1109/ICAL.2012.6308213.

[35] “Variable Stiffness Orthosis – Neurobionics Lab.” https://neurobionics.engin.umich.edu/research/wearable-robotics/variable-stiffness-orthosis/ (accessed Jul. 21, 2020).

[36] “Products,” *humotech*. https://www.humotech.com/products (accessed Jul. 20, 2020).

[37] S. P. Timoshenko, “9.61 Strain Energy and Castigliano’s Theorem,” in *History of Strength of Materials - With a Brief Account of the History of Theory of Elasticity and Theory of Structures*, Dover Publications.

[38] M. Ashby and D. Cebon, “Materials selection in mechanical design,” *J. Phys. IV Colloq.*, vol. 03, no. C7, pp. C7-1-C7-9, 1993, doi: 10.1051/jp4:1993701.

[39] “Sealing Application Defining Factors.” https://www.mnrubber.com/Design_Guide/6-2.html (accessed Aug. 11, 2020).

[40] B.-H. Cho, H.-W. Lee, and J.-S. Oh, “Estimation technique of air content in automatic transmission fluid by measurign effective bulk modulus,” 2002. /paper/Estimation-technique-of-air-content-in-automatic-by-Cho-Lee/9bb10824a0488b80b5443acc6d16d3dda98c8d76 (accessed Aug. 17, 2020).

Appendices

Appendix A: Proof of Concept

A low-fidelity prototype of the Autotuner was developed for a constant cross-section beam (Figure 43). The stiffness of the device at four effective beam lengths ($0.15\ m, 0.20\ m, 0.25\ m, 0.3\ m$) was measured by rotating the stage about a pin joint and measuring the required torque at different angular positions. Data was plotted against the theoretical range of solutions accounting for variance in the Young's Modulus of the beam material (HDPE) (Figure 44). The results proved the viability of the cantilever beam concept.

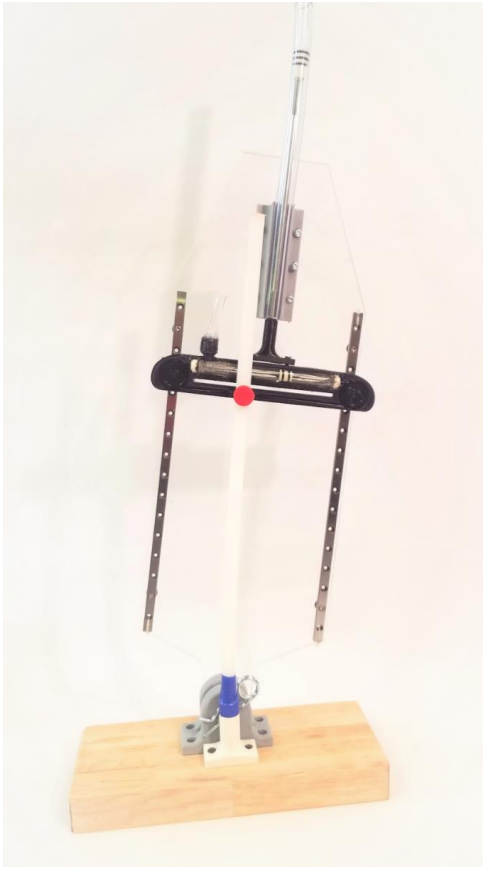

Figure 43: Low-fidelity prototype of the Autotuner.

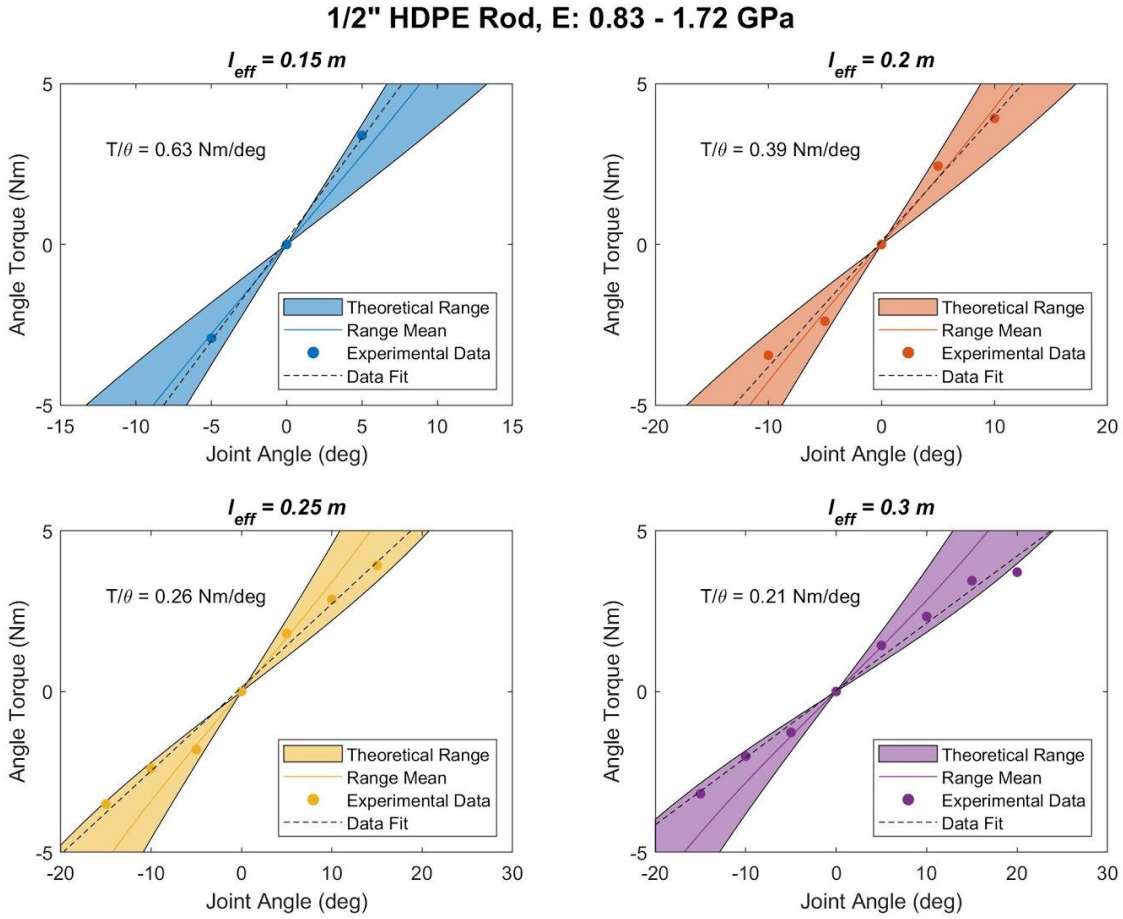

Figure 44: Stiffness data results from proof-of-concept testing.

Appendix B: Optimization Results

The beam design optimization resulted in an I-beam with varying thickness defined by Figure 45. The resulting stiffness curve is provided in Figure 46.

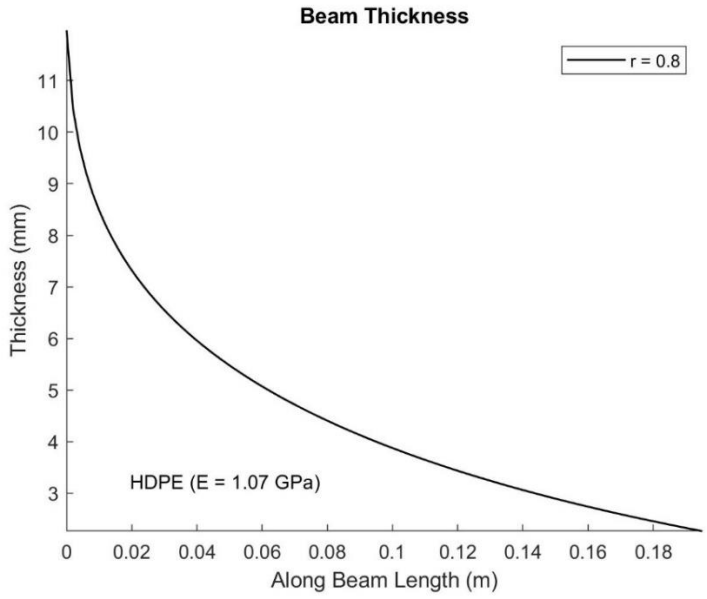

Figure 45: Thickness profile calculated using the beam optimization.

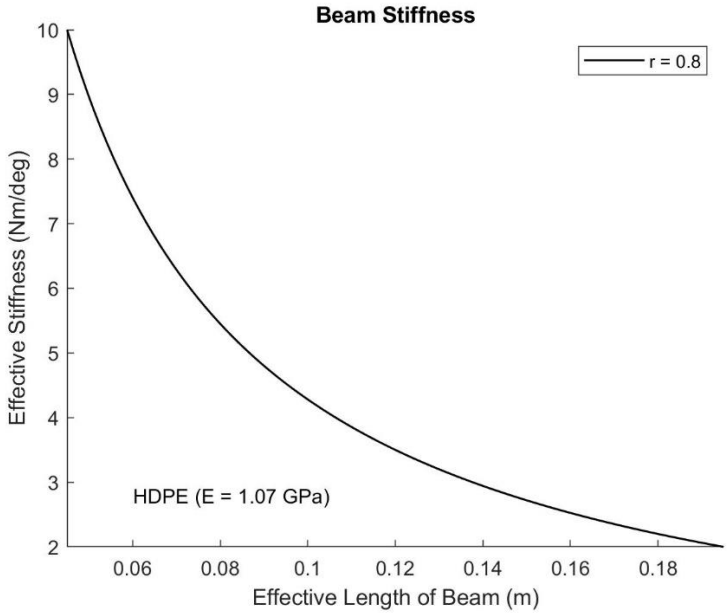

Figure 46: Stiffness v. beam length relationship for the optimized I-beam.

Appendix C: Bill of Materials

	Description	Supplier/Number	Material	Mass (g)	#	% Total Mass
			Exoskeleton Subassembly			
E-1	Limb Mount	Custom	Polycarbonate	14.97	1	7.06
E-2	Beam	Custom	HDPE	26.76	2	12.62
E-3	Load Point	Custom	7075-T6 Al	0.69	1	0.33
E-4	Beam Mount	Custom	Polycarbonate	35.46	1	8.36
E-5	Foot Plate	Custom	LDPE	4.67	1	1.10
E-6	Vertical Rail	McMaster-Carr/8381K560	Steel	20.41	2	9.62
E-7	Horizontal Rail	McMaster-Carr/8381K560	Steel	13.61	2	6.42
E-8	Rail Carriage	McMaster-Carr/8381K560	Steel	4.41	4	4.16
E-9	Mounting Screws	McMaster-Carr/ 92855A836	Steel	0.18	20	0.85
			Transmission Subassembly			
T-1	Horizontal Cylinder	Custom	7075-T6 Al	26.43	2	12.46
T-2	Vertical Cylinder	Custom	7075-T6 Al	34.26	2	16.15
T-3	Cylinder Piston	Custom	7075-T6 Al	1.81	4	1.71
T-4	Cylinder Cap	Custom	7075-T6 Al	3.75	8	7.07
T-5	Cable Retainer	Custom	7075-T6 Al	0.36	8	0.68
T-6	Vertical Pull	Custom	ABS	0.10	2	0.05
T-7	Cylinder Mount	Custom	ABS	5.78	2	2.73
T-8	Pulley Mount	Custom	ABS	0.18	2	0.08
T-9	Cable	McMaster-Carr/34235T26	Steel/Nylon	0.10	1	0.02
T-10	Set Screw	McMaster-Carr/91210A038	Steel	0.07	8	0.13
T-11	Pulley	McMaster-Carr/3434T310	Acetal	0.14	22	0.73
T-12	Hose Fitting	Jagwire/HFA401	Unknown	-	8	-
T-13	Hose	Jagwire/PRO	Kevlar	-	8	-
T-14	Seals	MN Rubber/001, 011, 013	70 Rubber	0.01	32	0.08
			Hip Pack Subassembly (Partial)			
H-1	Pump	Hydro Leduc/PB32	N/A	330	1	610 g total (1.34 lbs)
H-2	Valve	The Lee Co/ SDBB3321003A	N/A	70	4	

Appendix D: Part Specifications

Miniature Pump

Fixed displacement micropumps PB32 -PB32.5 -PB33 -PB33.5 -PB33HP

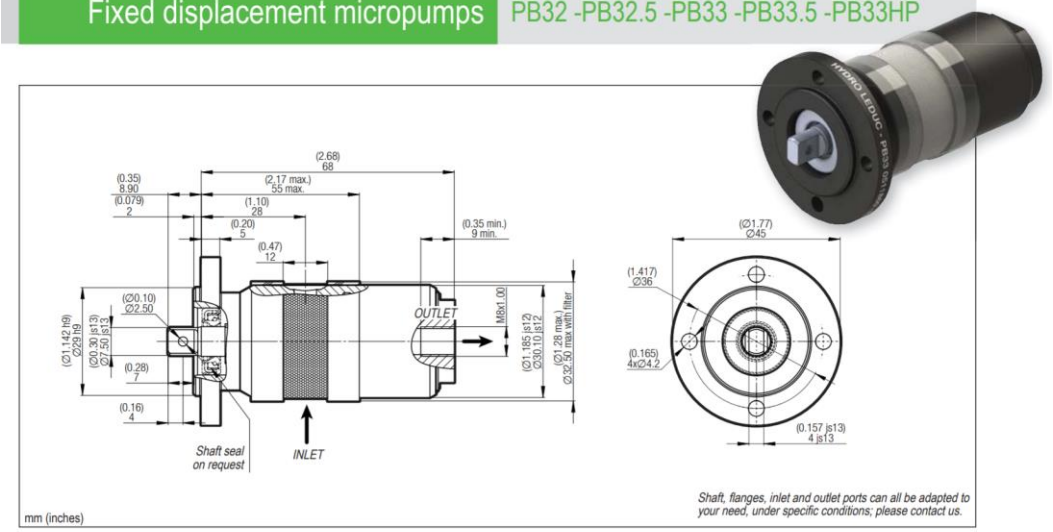

Characteristics

Type of pump		Displacement		Direction of rotation	Max. rotating speed (rpm)		Max. pressure			
					continuous		continuous		peak	
		mm³	Cu.in			peak	bar	PSI	bar	PSI
PB32	0518110	12	0.0007	CW & CCW	5000	6000	300	4350	350	5075
	0523370	20	0.0012		5000	6000	300	4350	350	5075
	0523380	25	0.0015		5000	6000	300	4350	350	5075
PB32.5	0511860	45	0.0027		5000	6000	300	4350	350	5075
PB33	053220	45	0.0027	CCW	5000	6000	300	4350	350	5075
PB33.5	057000	70	0.0042	CCW	5000	6000	300	4350	350	5075
PB33 HP	054560	45	0.0027	CW	5000	6000	900	13050	1000	14500

Solenoid On-off Valves

2-Way High Flow Solenoid Valve
SDBB3321003A

Single Coil Lead Wire Model

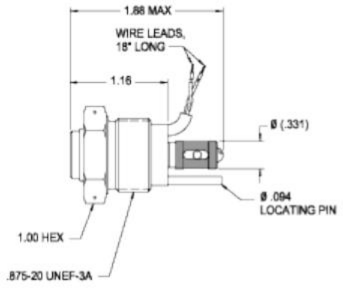

Installation View 1

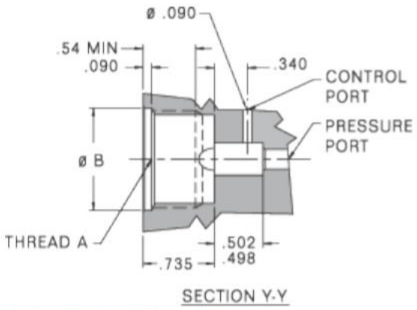

Installation View 2

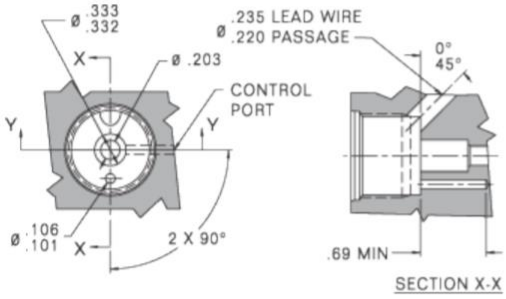

Valve Cutaway

SPECIFICATIONS	
Nominal System Pressure (psi)	3000
Number of Coils	Single Coil
Configuration	2-way N.C.
Lohm Rate	200
Screen Hole Size	.004 inches nominal
Weight	.15 lbs. max.
Operating Temperature: Ambient:	-65ºF to 275ºF
Operating Temperature: Fluid:	-65ºF to 275ºF
Leakage: Internal:	2 cc/minute max. at rated pressure
Leakage: External:	0 cc
Test Fluid	Skydrol
ELECTRICAL SPECIFICATIONS	
Current Drain:	0.28 amps at 28 Vdc at 70ºF (7.8 Watts)
Max. Operating Voltage:	32.2 Vdc
Pull-In Voltage:	18 Vdc max. at 275ºF and rated pressure
Minimum Drop Out Voltage:	3.0 Vdc at 70ºF and 3000 psi
Resistance:	92-108 Ohms at 70ºF
Response Time: Pull-In (at max. working pressure):	0.03 seconds max
Response Time: Drop-out (at max. working pressure):	0.03 seconds max
Stabilization Temperature:	235ºF max. with 28 Vdc applied, suspended in 70ºF to 110ºF still air, continuously energized
Insulation Resistance:	100 Megohms min. with 500 Vdc applied for 60 seconds
Dielectric Strength:	1500 Vrms min. at 60 Hz for 60 seconds
MATERIALS	
Body and Housing:	15-5 PH CRES/AMS 5659
Multi-Seal:	Polyamide-Imide/AMS 3670
Pin:	440C CRES/AMS 5630
Spring:	302 CRES/AMS 5688
Flanges, Plungers and Cover:	Si Iron BFM/ASTM-A867
Filter Screen Assy:	304L CRES/ASTM A 666
Bobbin:	304L CRES/AMS-QQ-S-763
Seal:	Graphite Filled PTFE
Shaft:	440C CRES/AMS-QQ-S-763
Retainer:	2024 T-351 AL/AMS-QQ-A-225/6
Retaining Ring:	302 CRES/ASTM A313/A313M
Coil:	Copper Magnet Wire/NEWA MW 1000
Lead Wire:	22 AWG/SAE AS22759/11-22
Separator:	ARAMID 410/MIL-1-24204
Shrink Tube:	MIL-DTL-23053/8 & /12
Insulation Tape:	Kapton, Polyimide/ASTM D5213
Solder:	Sb05A/J-STD-006
Braze:	AMS 4774
Potting Compound:	Stycast 2762FT, Catalyst 17
Front Electrical Connection	Lead Wire Version
FINISH	
Cres Parts:	Passivated
Soft Magnetic Material:	Nickel Plate/AMS 2404

Miniature Linear Rails

Miniature Ball Bearing Carriage and Guide Rail

with 6 mm Wide x 120 mm Long Rail

$155.74 Each
8381K56

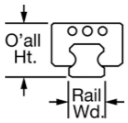

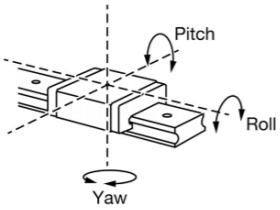

Moment Loads

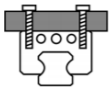

Load Fastening from Top

Carriage and Guide Rail Type	Ball Bearing
Carriage Profile	Standard
Bearing Type	Ball
Load Fastening	From Top
For Rail Width	6 mm
Rail Length	120 mm
Rail Height	2.8 mm
Dynamic Load Capacity	95 lbs.
Static Load Capacity	180 lbs.
Static Pitch Moment Load Capacity	1.3 ft.-lbs.
Static Roll Moment Load Capacity	1.8 ft.-lbs.
Static Yaw Moment Load Capacity	1.6 ft.-lbs.
Overall Height	4.5 mm
Carriage Width	12 mm
Carriage Length	20 mm
Carriage Material	440 Stainless Steel
Rail Material	440 Stainless Steel
Bearing Material	440 Stainless Steel
Maximum Temperature	210° F
Carriage Mounting	
Number of Holes	2
Hole Thread Size	M2
Hole Thread Pitch	0.4 mm
Hole Depth	1.6 mm
Fasteners Included	No
Guide Rail Mounting	
Number of Holes	8
For Fastener Thread Size	M2
Hole Center-to-Center	15 mm
Hole-Center to End	7.5 mm
Hole Depth	1.3 mm
Fasteners Included	Yes
Lubrication	Lubricated
Lubricant	Grease with Lithium Thickener
RoHS	RoHS 3 (2015/863/EU) Compliant
REACH	REACH (EC 1907/2006) (06/25/2020, 209 SVHC)

Appendix E: Seal Design

The seals used in the hydraulic cylinders were designed using guidelines outlined by MN Rubber [39]. The radial clearance defined by Figure 47 and Figure 48 was selected for a 3000 psi system and 70 durometer rubber.

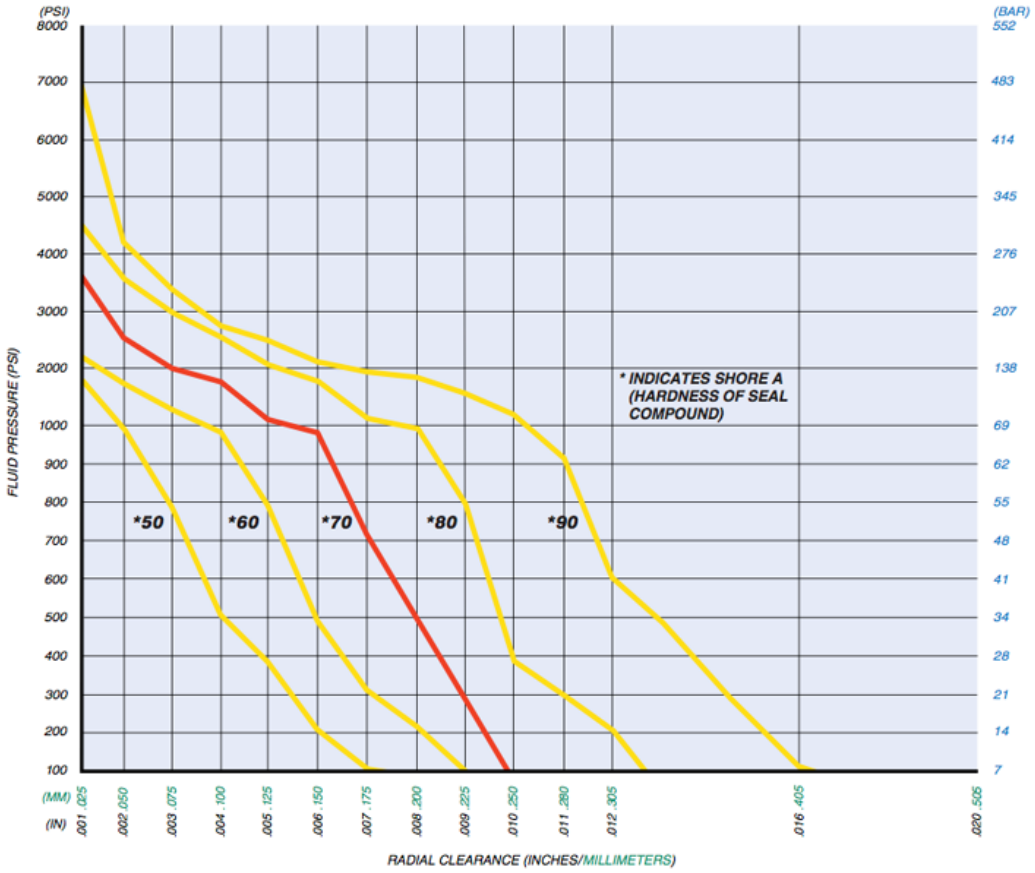

Figure 47: Radial clearance guidelines for varying fluid pressures and sealing materials.

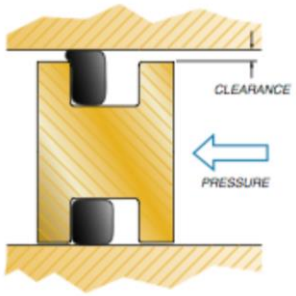

Figure 48: Definition of radial clearance in this sealing application.